Materials & Design 260 (2025) 114985

Contents lists available at ScienceDirect

Materials & Design

journal homepage: www.elsevier.com/locate/matdes

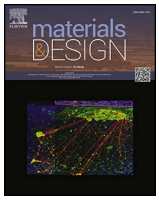

In-situ Dynamic laser area heating during diode point melting for thermal gradient reduction in laser powder bed fusion

Alkim Aydin [a,b,c,*], Erhan Cetin [a,d], Kamran Mumtaz [a]

[a] School of Mechanical, Aerospace and Civil Engineering, The University of Sheffield, Sheffield, United Kingdom, S1 3JD
[b] Department of Automotive Engineering, Cukurova University, Adana, Türkiye, 01250
[c] Additive Manufacturing Technologies Research and Application Center - EKTAM, Gazi University, Ankara, Türkiye, 06560
[d] Department of Mechanical Engineering, Hitit University, Çorum, Türkiye, 19030

ARTICLE INFO

Keywords:
Additive Manufacturing
Ti6Al4V
Diode Point Melting (DPM)
Dynamic Laser Area Heating (DLAH)
Microstructure

ABSTRACT

Additive Manufacturing (AM) via Laser Powder Bed Fusion (LPBF) generates steep thermal gradients and rapid solidification rates (10^5–10^6 K/s) during processing. This can result in the formation of residual stresses and process defects such as cracking and warpage. Conventional thermal gradient mitigation techniques like substrate pre-heating or powder bed heating are energy-intensive, lack spatial precision, and compromise powder recyclability. This study introduces a novel in-situ Dynamic Laser Area Heating (DLAH) method, enabling spatially controlled surface heating up to 400 °C. The system uses a defocused 140 W, 915 nm diode laser with beam-homogenising optics, dynamically aligned to follow the melt pool. DLAH is integrated into a custom Diode Point Melting (DPM) platform that uses a 44 W, 450 nm laser for precision processing of Ti6Al4V powder. The addition of DLAH broadens the processing window by stabilising melt pools over wider scan speeds and energy densities. This enhanced thermal control suppresses stress-driven defects, achieving near-full density (99.99 %) and improved surface finish (Ra = 2.84 μm). Static heating rates reached ~30.6 °C/s, but during actual scanning, effective cooling rates varied with scan speed and DLAH overlap, allowing spatial modulation of solidification kinetics. Microstructural analysis revealed that DLAH induced coarser α′ martensite (average width ~ 3.0 μm vs < 2.6 μm) and reduced aspect ratios (2.4–2.5 vs > 2.8), with little change in lath length. These findings show that dynamic, localised thermal management enables control over microstructural features and mechanical properties, offering a scalable solution for improved process reliability and performance in metal AM.

1. Introduction

The Additive Manufacturing technique Laser Powder Bed Fusion (LPBF) uses a high-power rapidly moving laser to melt powdered feedstock and create high-density near-net-shape 3D components from a variety of metallic alloys. Despite the many advantages of LPBF (e.g. design freedom for complex geometries, geometric customisation, material efficiency etc.), the process has several challenges such as high investment and operating costs, scalability limitations, and post-processing operations.

One of the major challenges associated with LPBF is the significant thermal gradients that arise during the rapid laser melting and solidification of powdered feedstock. These thermal gradients can create residual stresses that can lead to geometric warping/distortion during or after printing, micro-cracks and the requirement for post-processing heat-treatment operations that increase part production time and cost [1,2]. Furthermore, the high energy input from the laser and the rapid cooling rates can result in significant thermal distortions and a rough surface finish, necessitating extensive post-processing to achieve the desired surface quality and dimensional tolerances. Elevated thermal gradients in LPBF enhance Marangoni-driven convection and destabilize the melt pool by amplifying capillary and buoyancy instabilities, leading to uneven solidification tracks, such as balling and ripples, which manifest as increased surface roughness in the as-built part [3,4].

To mitigate these issues, researchers have explored integrating substrate heating systems that raise the temperature of the entire powder bed in order to reduce thermal gradients. Caprio et al. [5] introduced an inductive high-temperature LPBF system for highly crack-susceptible Ti–48Al–2Cr–2Nb alloy, using a pre-heating temperature of 800 °C and a controlled cooling rate of 5 °C/min after fabrication. This

* Corresponding author at: School of Mechanical, Aerospace and Civil Engineering, The University of Sheffield, Sheffield, United Kingdom, S1 3JD.
E-mail address: alkaydin@gmail.com (A. Aydin).

https://doi.org/10.1016/j.matdes.2025.114985
Received 23 June 2025; Received in revised form 15 October 2025; Accepted 20 October 2025
Available online 22 October 2025

approach effectively minimized crack formation and resulted in a density exceeding 99 %. Ali et al. [6] developed a customised powder bed that enabled up to 770 °C substrate heating during LPBF of Ti6Al4V. Their investigation demonstrated a pronounced reduction in residual stresses and notable improvements in mechanical performance. Specifically, a 3.2 % increase in yield strength and a 66.2 % enhancement in ductility were reported. Residual stress measurements indicated a progressive decline with increasing preheat temperature: a 71 % reduction at 370 °C and an 88.3 % reduction at 470 °C, relative to the baseline 100 °C condition. At and above 570 °C, residual stresses were effectively eliminated, with some instances showing the presence of beneficial compressive stresses, which may contribute to improved fatigue resistance. The pre-heating facilitated the decomposition of the martensitic structure into an α + β equilibrium phase, further enhancing both strength and toughness, making the process highly beneficial for structural applications. Buchbinder et al. [7] systematically examined preheating effects on distortion in aluminium components produced by LPBF. They found that starting from a pre-heating temperature of 150 °C, thermally induced residual stresses were significantly reduced, and at 250 °C, distortion was eliminated entirely. The process also prevented stress-induced cracks, ensuring defect-free production of AlSi10Mg parts, thus making the process reliable for high-precision manufacturing. Gussone et al. [8] investigated the influence of preheating during LPBF of γ-TiAl, showing a minimization in aluminium evaporation and promoted direct solidification into the α phase. This led to a fine near-lamellar (α_2/γ) structure with fewer defects. Pre-heating not only stabilized the microstructure but also reduced thermal stresses, minimizing macro-cracks and enhancing mechanical properties after post-processing, such as hot isostatic pressing, which further improved part reliability. Papadakis et al. [9] compared three preheating methods that included chamber pre-heating, base-plate heating, and laser pre-scanning heating. They found that laser pre-scanning is more energy-efficient for low-volume parts due to reduced energy input. However, chamber and base-plate pre-heating are more effective for high-volume or batch production utilisation more of the build volume, offering better control over thermal gradients and residual stresses for larger or multiple parts. These findings highlight the versatility of pre-heating approaches across different manufacturing scales and materials. Pre-heating is also particularly important in ceramic processing to reduce crack formation. This is because ceramics are highly susceptible to cracks due to thermal gradients caused by temperature differences, making pre-heating essential for minimizing these defects. [1011]. Table 1 provides a summary of the pre-heating effects in additive manufacturing, allowing for easy comparison of different methods and outcomes across various materials.

Unlike the aforementioned methods, pre-heating is also utilised in the Electron Beam Melting (EBM) technique. The primary reason for applying pre-heating in Electron Beam Melting (EBM) is to prevent the 'smoke effect,' which occurs when high-velocity electrons strike the powder bed, creating a negative charge buildup that causes particles to repel and eject due to electrostatic forces. Pre-heating mitigates this effect by pre-sintering the powder particles, forming weak interparticle bonds that stabilize the powder bed and improve its conductivity. This sintering step is critical for maintaining powder bed integrity during the process, ensuring consistent part quality [11]. The required pre-heating (sintering) temperature varies by material, typically ranging from 500 °C to 1000 °C in EBM processes. Consequently, EBM typically yields samples with slightly coarser microstructures and lower residual stresses compared to LPBF. As seen from the previous-mentioned studies, preheating has several positive effects, such as reducing cooling rates, lowering residual stresses within the material, promoting grain growth, and mitigating hot tearing. To reduce residual stress, the most commonly used techniques involve heating the powder bed or the substrate. However, heating the entire powder bed, rather than a specific region, requires substantial energy and allows no spatial control. Additionally, repeated heating can lead to issues such as sintering of the powder, adhesion between particles, and changes in chemical composition can affect the material's long-term recyclability [12]. Additionally heating the bottom of the powder via the substrate can result in a temperature gradient across the z-axis, with no method to directly heat at the top powder layer, the most critical when managing stress reduction.

Diode Point Melting (DPM) is a gantry scanned variant of powder bed fusion in which several low-power 450 nm diode emitters are optically combined into a single melt spot mounted on a traversing axis; this architecture exploits higher absorptivity at 450 nm, avoids galvo optics, and drives down laser hardware cost (source/power/cooling < $1500) while enabling larger scan fields than conventional 1064 nm LPBF, albeit at lower throughput. In the current setup, eight 5.5 W diodes were focused to a ~100 × 150 μm spot; DPM was deliberately run

Table 1
Preheating within LPBF systems.

Material	Technology for pre-heating	Pre-heating temperature	Key findings	Ref.
Ti-48-Al-2Cr-2Nb	Powder bedpre-heating	800 °C	Crack formation was reduced, resulting in a density exceeding 99 %. Cooling rate controlled at 5 °C/min, enhancing mechanical stability.	[5]
Ti6Al4V	Substratepre-heating	100 to 770 °C	Residual stress was significantly reduced, with a 3.2 % increase in yield strength and a 66.2 % improvement in ductility due to phase transformation from martensitic to α + β.	[6]
AlSi10Mg	Substratepre-heating	150 °C, 250 °C	Thermal stresses were reduced significantly, and distortion was eliminated at 250 °C. Pre-heating at this temperature also prevented stress-induced cracks, ensuring defect-free manufacturing.	[7]
γ-TiAl	Substratepre-heating	800 °C, 1000 °C	Pre-heating minimized macro-cracks and stabilized the microstructure into a fine near-lamellar (α_2/γ) structure. Mechanical properties improved significantly, especially after hot isostatic pressing.	[8]
AlSi10Mg, Ti6Al4V	Laser pre-heating	100 to 500 °C	Laser pre-scanning heating was more energy-efficient for small parts, while chamber and base-plate heating proved more effective for large-volume or batch production by better managing thermal gradients and residual stresses.	[9]
AlSi10Mg	Substrate pre-heating	160 °C	Cold platform resulted in higher supersaturation of Si, enhancing hardness and tensile properties after direct aging. Hot platform strategy reduced the aging response due to overaging effects.	[10]

slower than LPBF, yielding reduced thermal gradients and improved energy coupling, and in Ti-6Al-4 V achieved up to 99.41 % relative density at 38 W [13]. Microstructurally, the slower solidification fosters a stable α + β structure with prior-β grains ~ 30 × larger than LPBF and a correspondingly higher stiffness (Young's modulus) than as-built LPBF, consistent with reduced cooling-rate martensite formation. In exchange, as-built surfaces are rougher due primarily to the larger spot (Ra ≈ 25.4–39.5 μm in DPM vs 2.6–8 μm in LPBF) [13], Overall, relative to fibre laser galvo based LPBF, DPM trades speed and surface finish for markedly lower hardware cost, improved optical absorption, reduced thermal gradients, and more equilibrated (α + β) microstructures, while retaining the ability to reach near-full density when parameters are properly normalised and tuned.

In this study a new heating approach has been developed and integrated into an alternative to LPBF, Diode Point Melting (DPM) [13] a process that utilises a 450 nm diode laser attached to an x/y gantry system [14–17] that traverses the powder bed melting material layer by layer. The new Dynamic Laser Area Heating (DLAH) approach utilises a specially designed de-focused laser system that precisely follows the DPM laser through direct attachment to the x/y gantry system. This creates a square heating area (100 mm^2) centred to the DPM laser on the powder bed. This in-situ dynamic heating approach removes the requirement for an entire powder bed to be pre-heated, directly laser heating the top layer of a powder bed with capacity for spatial temperature control through real-time adjustment of DLAH laser power. This provides heat before DPM melting (pre-heat) followed by heating after the melt pool has formed (post-heating) due the 10x10mm square pre-heat area centred precisely around the 100x150um DPM laser spot (described in more detail in section 2.2).

2. Material and method

2.1. Material

In this study gas atomised Ti6Al4V Grade 23 powder provided by Carpenter Additive was used. The particles display a spherical shape and have a size range of 15–45 μm. Based on the manufacturer's measurements, which are conducted following the ASTMB822 standard, the size distribution quantiles are as follows: D_{10} = 17.4 μm, D_{50} = 30.8 μm, and D_{90} = 51.6 μm[13]. The particle size distribution graph and Scanning Electron Microscopy (SEM) image of Ti6Al4V powder are presented in Fig. 1. It is evident that the particles predominantly exhibit spherical morphology, with a small proportion of irregular near-spherical particles present. According to the manufacturer's test report, the apparent density is 2.21 g/cm3, and the hall flowability, as determined by the ASTM B213 standard, is 37.00 s/50 g. Ti6Al4V substrate plates were used to build the DPM components. Table 2 shows the composition of elements calculated by the ASTM F3001 method in the Ti6Al4V powder material and Table 3 shows the physical properties of the same powder.

2.2. System development

2.2.1. Diode Point melting (DPM) and Dynamic laser area heating (DLAH)

The DPM and DLAH lasers are both connected to a gantry movement system. Gantry system and DPM laser are controlled by a computer and DLAH is controlled by laser diode controller. Fig. 2 illustrates the schematic of the experimental setup. With the movement of the gantry system, this dual laser system can melt and/or heat at the desired region. The DPM laser is shown schematically in Fig. 3a. and consists of eight individual 450-nm diode emitters (≈5.5 W each; 44 W total) are optically combined and conditioned to produce an elliptical focal spot of 100 × 150 μm at normal (vertical) incidence. When the optical head is tilted by 45° about the minor (100 μm) axis, the projected major diameter becomes 100 × 212 μm. The available optical power remains 44 W; hence the peak irradiance decreases in proportion to the increase in illuminated area (≈1.18 × 10^4 $μm^2$ → ≈1.67 × 10^4 $μm^2$, ~1.41 × larger). The DLAH laser is shown in Fig. 3b., it consists of a de-focused 140 W diode laser (915 nm wavelength) heating at the powder bed a 10x10mm square area. The DLAH diode laser is coupled to a fibre that enters the DLAH laser head, the laser passes through a collimating lens, beam homogeniser and de-focusing lens. A beam homogeniser was employed to convert the native Gaussian intensity profile into a top-hat distribution, ensuring uniform irradiance across the beam cross-section. This spatial uniformity minimises localized overheating and thermal gradients, leading to more consistent melt pool behaviour, reduced residual stress formation, and enhanced microstructural homogeneity during laser-material interaction. The beam conversation is shown schematically in Fig. 3c.

Due to the methodology employed and hardware setup, both the DLM and DLAH lasers would be position at angles to each other but focused on the same area on the powder bed. This would create different angles of laser irradiation relative to the substrate which would change or distortion DLM and DLAH beam profiles at the powder bed. To examine its influence four different laser setups were used, as shown in Fig. 4. In Case-1, only the DPM laser is used and is position in an inclined (45° degrees from vertical), with no DLAH laser active. In Case-2, both the DPM and DLAH lasers are used, with the DPM laser inclined and the DLAH laser perfectly vertical relative to the powder bed. In Case-3, similar to Case-1, only the DPM laser is used, but it is positioned vertically. Finally, in Case-4, both the DPM laser and the DLAH laser are active, with the DPM laser vertical and the heating laser inclined.

For all cases, the lasers referred to as "inclined" are positioned at an

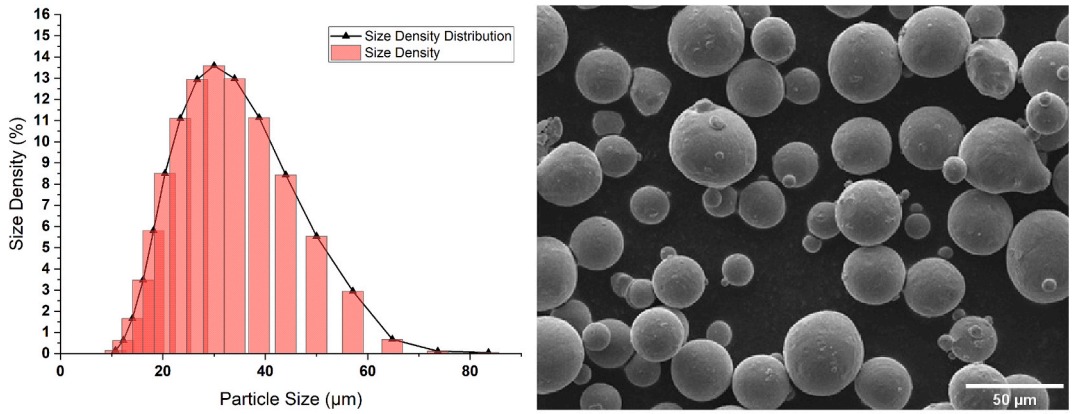

Fig. 1. A) powder size distribution graph and b) sem image of ti6al4v.

Table 2
Chemical composition of elements in the Ti6Al4V powder material supplied by Carpenter Additive.

Ti	Al	V	O	N	H	Fe	C	Others
Balance (wt. %)	5.91	3.88	0.07	0.01	0.002	0.19	<0.01	0.40

Table 3
Physical properties of the Ti6Al4V powder feedstock [13,18].

Material	Ti6Al4V Powder
Absorptivity (A)	0.72 (450 nm wavelength)
Thermal conductivity (λ)	7.2 W/m.K (at 298 K)
Material density (p)	4420 kg/m^3
Specific heat (C_P)	560 J/kg.K in (283–923 K)

angle of 45° from the vertical, while the lasers refer to as "vertical" are positioned directly above the powder bed at 0° from the vertical. The DLAH laser and DPM laser are synchronized to turn on and off simultaneously. The DLAH laser is defocused and uses specialized beam-shaping optics to convert its Gaussian beam profile into a top-hat profile. With the top-hat profile, a uniform temperature distribution is achieved when positioned vertically as shown in Fig. 5. As the DLAH laser is position 30°-45° from the vertical, the uniformity of the beam energy distribution across the heating area changes, its significance during processing will be examined.

The DPM laser has a Gaussian beam characteristic, when the DPM laser is positioned vertically, the laser beam is circular, when positioned at an incline position, the beam profile becomes elliptical. Fig. 6 shows how a pre-heat and post-heat zone generated by the DLAH laser surrounds and moves precisely with the generated DPM melt pool. Fig. 7, shows the influence on heating area and maximum heating temperature at the powder bed when changing the focal length of the DLAH laser relative to the powder bed. A FLIR C5 thermal camera was used to measure the heated area and compute the area-averaged surface temperature (≤400 °C). To obtain a representative point estimate and assess spatial uniformity, an Optris CTVideo 3 M pyrometer acquired five spot readings per experiment; centre, top-left, top-right, bottom-left, and bottom-right, where the five values were averaged to yield a pyrometric mean and compared with the camera-derived average (with emissivity and reflected-temperature corrections applied). When the DLAH focal length was set at 150 mm, the heating area was 15.0x15.0 mm^2 with the powder reaching a maximum surface temperature of 200 °C and was deemed too low a surface temperature for this study. One slightly more focused to 90 mm focal length, the heating area reduces to 10.0x10.0 mm, however the maximum powder temperature doubles to 400 °C. At a focal length of 90 mm, the dynamic laser assisted heating (DLAH) system produced a powder heating rate of 30.6 °C/s and a cooling rate of 19.6 °C/s when held stationary. It should be noted that these values were obtained under static conditions; during actual processing, the translational motion of the DLAH laser is expected to decrease the heating rate and increase the cooling rate, depending on the scanning speed. The influence of laser movement on thermal transients is further examined in subsequent sections.

In the first part of this study, single layer Ti6Al4V samples are produced solely with DPM using different laser irradiation angles relative to the powder bed (vertical and 45° to vertical) The DPM will process Ti6Al4V powder at scanning speeds of 120, 1200, 1800, 2400, 3000, 3600, 4200, and 4800 mm/min. From preliminary trials when the laser speed exceeded 4800 mm/min, the density of the samples decreased significantly due to lack of fusion, therefore scan speed values above this are not considered exceeded. However, at speeds of 1200 mm/min and below, no significant differences are observed with across the melt pool until approximately 120 mm/min. Therefore, only one scan speed below 1200 mm/min (120 mm/min) is shown the results, followed by increments of 600 mm/min up to a maximum value of 4800 mm/min. Additionally, the laser power, hatch distance, and layer thickness values are kept constant at 45.5 W, 100 μm (33 % overlap), and 1000 μm (to measure melt pool penetration depth), respectively. Prior to processing,

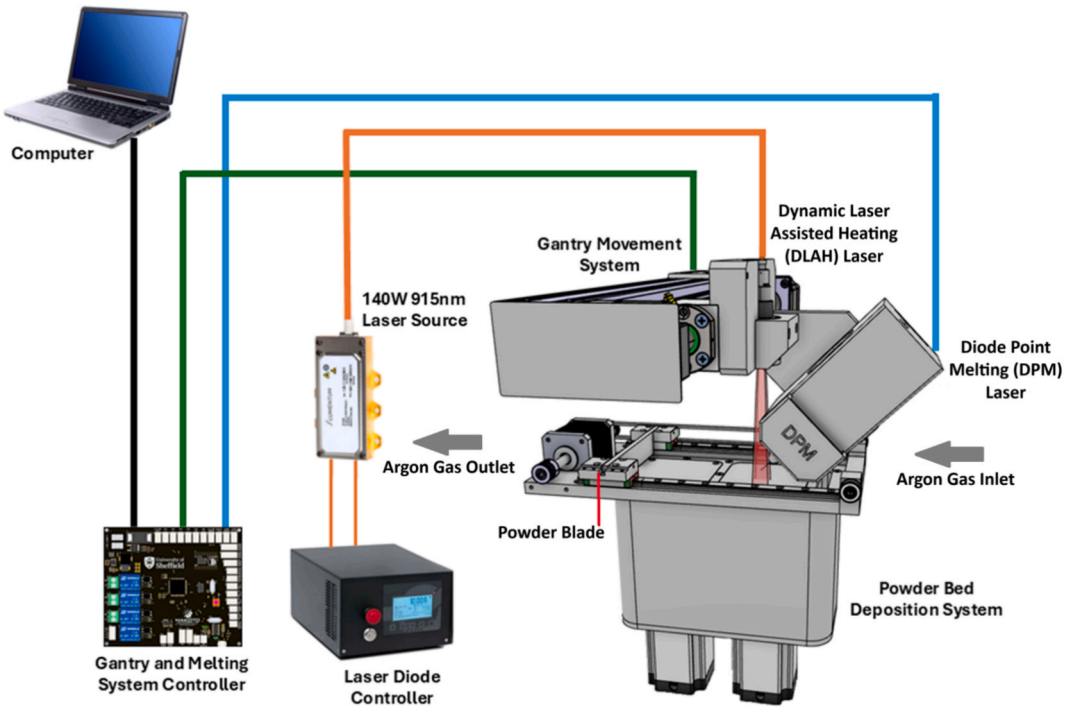

Fig. 2. Schematic of the DPM and DLAH.

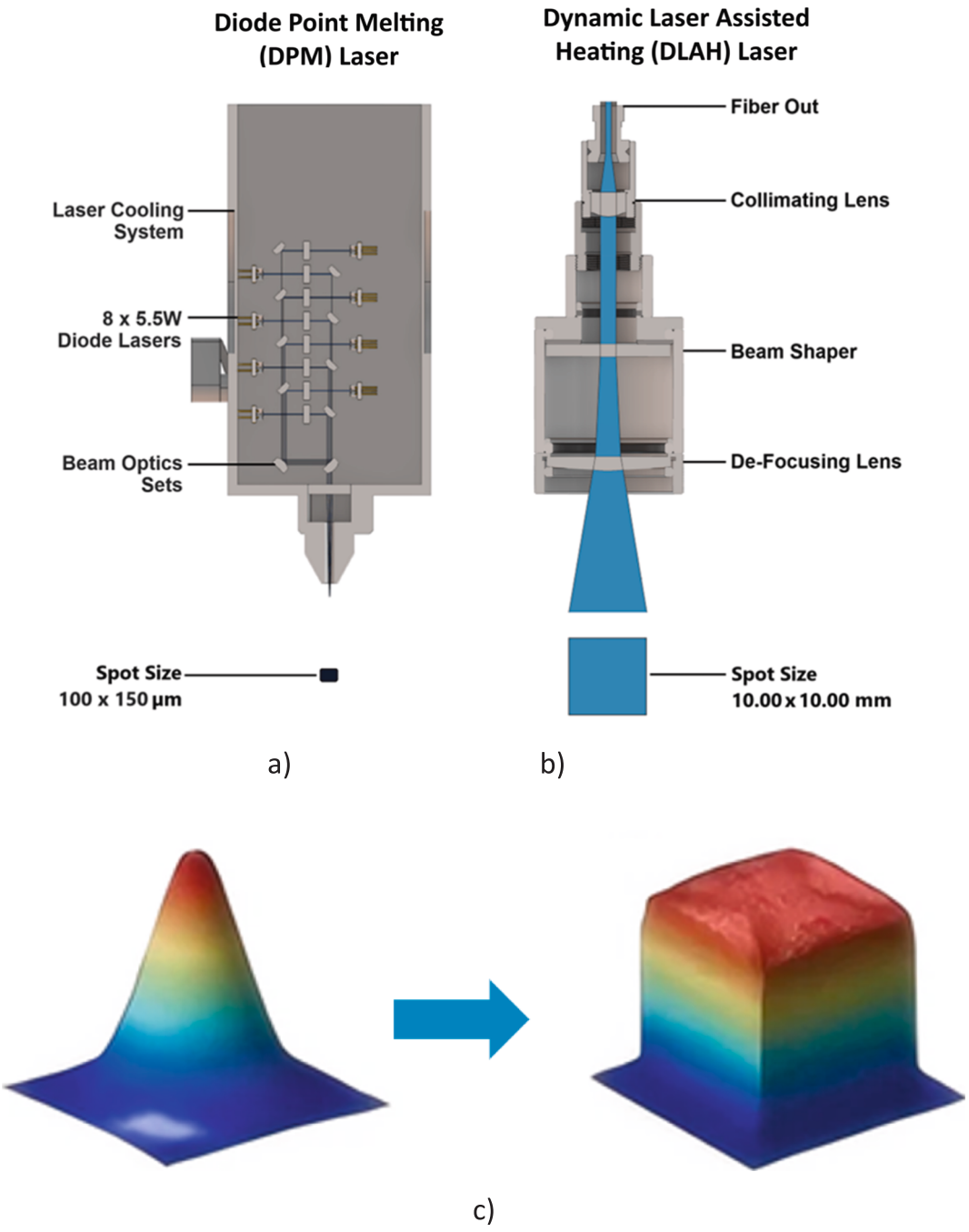

Fig. 3. The schematic view of a) DPM laser, b) DLAH laser and c) beam homogenisation from gaussian beam to top-hat beam.

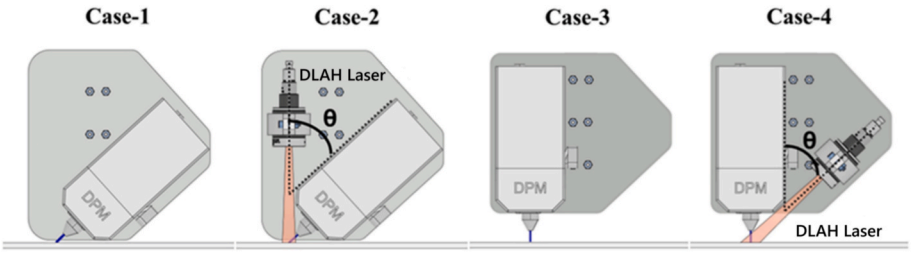

Fig. 4. The DPM and DLAH laser positions used during this study.

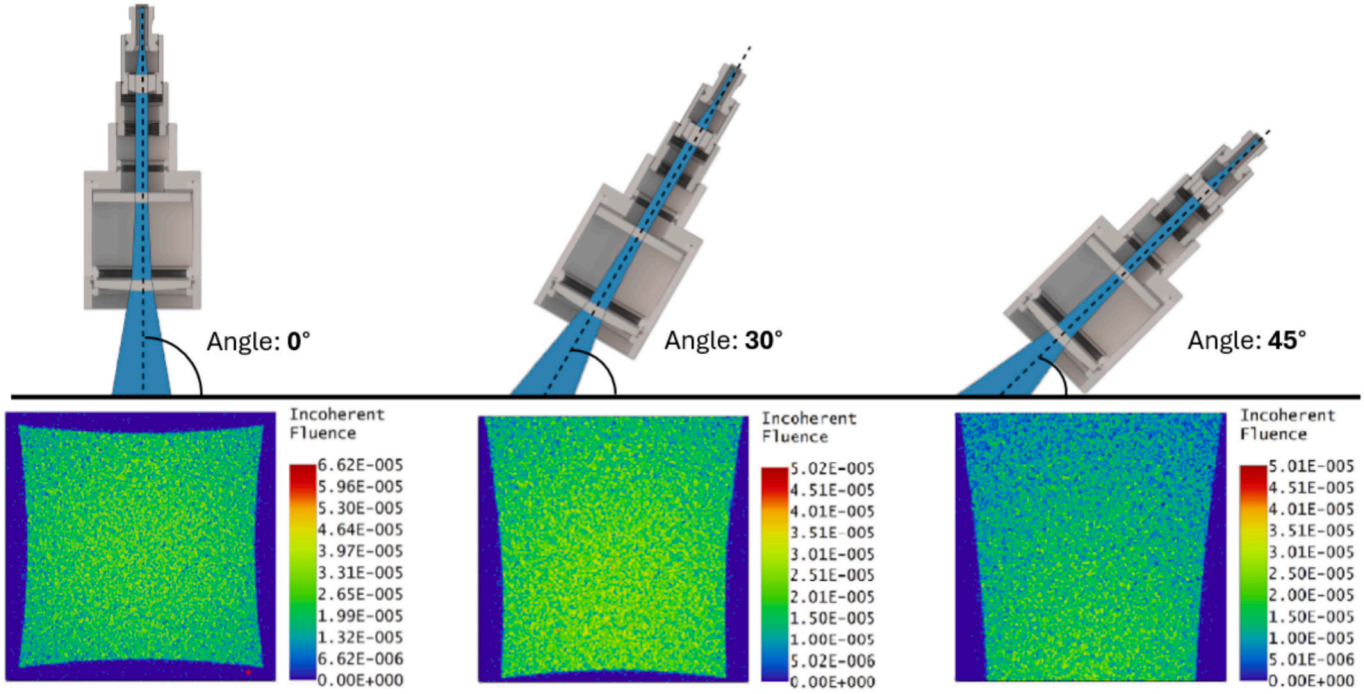

Fig. 5. DLAH 10x10mm laser beam characteristics at different angles from the vertical.

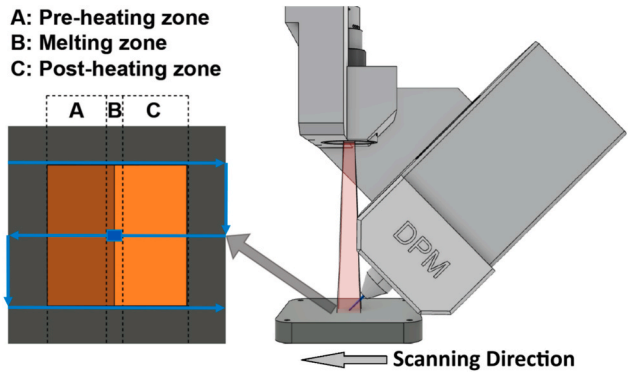

Fig. 6. The effect of movement of DPM & DLAH on top surface of powder bed, creating pre heating in front of DPM laser, Zone A. DPM laser melting region in the centre of Zone B and post heating Zone C that encapsulated the solidifying melt pool generated within Zone B.

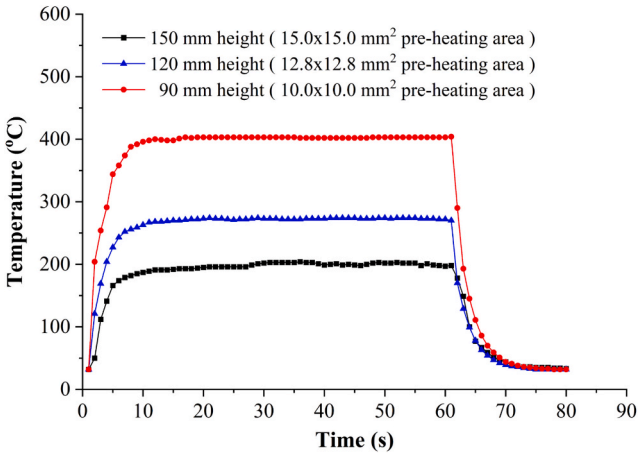

Fig. 7. Temperature-time graphs according to DLAH laser in stationary position for different heights.

the chamber is purged with argon gas until the oxygen concentration dropped below 0.1 %. An oxygen sensor is used to continuously monitor and ensure that the oxygen level remain stable throughout the procedure.

2.2.2. *Statistical Analysis: Full factorial Three-Way ANOVA*

To statistically evaluate the influence of process parameters and their interactions on key material responses, a full factorial three-way analysis of variance (ANOVA) was applied [19]. The design incorporated three factors: scanning speed (8 levels), DPM laser angle (2 levels: vertical/inclined), and heating condition (2 levels: on/off). The response variables examined were relative density and surface roughness. This comprehensive approach allowed quantification of both main effects and interaction effects (two-way and three-way) on the measured outputs. Each combination of factors was evaluated across the experimental space ($2 \times 2 \times 8 = 32$ runs), and statistical models were developed using ordinary least squares (OLS) regression.

The ANOVA revealed that scanning speed had the most statistically significant main effect on both relative density and surface roughness. Heating presence and laser angle also showed notable effects, particularly under higher speed conditions. Significant interaction terms were observed, indicating that the influence of one factor (e.g., heating) varied depending on the level of another (e.g., angle). These statistical insights supported the identification of optimal parameter combinations and underscored the complex interdependencies present in hybrid diode melting and heating techniques.

2.3. *Material Preparation*

DPM processed samples are embedded in bakelite using a Buehler Simplimet Mounting Press before optical microscope examination. After bakelite process, the samples are grinded and polished using a Buehler Automet machine. The grinding process is performed sequentially with 60, 320, 600, 1200, 2400, and 4000 grit papers. Before transitioning to each successive grit paper, the samples are rinsed with water and

cleaned with isopropanol. Following grinding process, polishing is employed using 1 μm colloidal suspension solution.

2.4. Material Characterization

The surface roughness, single layer relative density and melt pool characteristics of the Ti6Al4V samples are investigated in detail in this work. Measuring surface roughness during single layer DPM + DLAH trials is essential for evaluating the quality of powder melting, surface remelting uniformity, and scan strategy effectiveness. Surface roughness directly influences powder recoating in subsequent layers; excessive roughness can disrupt powder spreading, cause uneven layer thickness, and introduce porosity or lack-of-fusion defects. By assessing roughness at the single layer stage, it becomes possible to optimise key process parameters such as laser power, scan speed, hatch spacing, and scan strategy before initiating multi-layer builds. This ensures improved layer-to-layer consistency, reduces defect accumulation, and enhances final part quality and dimensional accuracy. Important parameters for assessing surface roughness include Ra, Rq, and Rz, which provide essential insights into the surface's roughness and profile characteristics [20,21]. This study specifically utilized the Ra value, calculated using the following formula.

$$Ra = \frac{1}{L}\int_0^L |Z(x)|dx \tag{1}$$

where L represents the sampling length and $Z(x)$ denotes the height of the profile at position x. The top surface roughness of the manufactured samples is analysed optically using the Alicona Infinite Focus SL system. In addition, Nikon optical microscopy is used to determine the melt pool characteristics under 5x magnification. The sample microstructure is also captured using a Tescan Vega3 SEM machine and X-ray Diffraction (XRD) data captured from Panalytical Aeris X-Ray Diffractometer machine. Following the images captured from optical microscopy and SEM machine, Image J software is used to calculate the melt pool depth and relative density of the samples. This image correlation software significantly reduced calculation time compared to the Archimedes method [22,23], particularly when handling multiple samples, by consistently applying the same threshold values to ensure more accurate results.

The normalised energy density (NED) formula [13,24] is used for all analyses in this work and corresponding formula is given as follows.

$$\mathrm{NED} = \mathrm{E_n} = \frac{q^*}{v^* l^* h^*} \tag{2}$$

$$q^* = \frac{A\,x\,q}{r_B \lambda\,(T_M - T_0)}, \quad v^* = \frac{v\,r_B}{\alpha}, \quad l^* = \frac{2l}{r_B}, \quad h^* = \frac{h}{r_B} \tag{3}$$

$$\mathrm{NED} = \mathrm{E_n} = \frac{q^*}{v^* l^* h^*} = \left[\frac{\frac{A\,q}{r_B\,\lambda\,(T_M - T_0)}}{\frac{v\,r_B}{\alpha}\;\frac{2l}{r_B}\;\frac{h}{r_B}}\right] = \left[\frac{A\,q\,\alpha}{2\lambda\,v\,l\,h\,(T_M - T_0)}\right] \tag{4}$$

$$\alpha = \frac{\lambda}{p\,C_P} \tag{5}$$

$$\mathrm{NED} = \mathrm{E_n} = \frac{q^*}{v^* l^* h^*} = \left[\frac{A\,q}{2\,v\,l\,p\,h\,C_P\,(T_M - T_0)}\right] \tag{6}$$

where A represents absorptivity, q denotes laser power (W), α is thermal diffusivity (m^2/s), v is scanning speed (m/s), l indicates layer height (m), p is material density (kg/m^3), h refers to hatch distance (m), C_p is the specific heat capacity of the powder (J/kgK), T_m is the melting temperature of the powder (K), T_0 is the powder bed temperature (K), r_B is the laser beam spot radius (m), and λ represents thermal conductivity (W/mK).

3. Results and discussion

3.1. Defects of the Ti6Al4V samples

Literature studies on LPBF systems typically identify three fundamental defects mechanisms: keyholing, balling, and lack of fusion [25,26]. These mechanisms are directly related to scanning speed and laser power. The keyhole mechanism generally occurs at low scanning speeds and high laser power, lack of fusion at high scanning speeds and insufficient laser power. Some selected defects of samples formed during DPM processing are shown in Fig. 8 for different process parameters. Lack of fusion (LOF) in powder-bed processes arises when the local volumetric energy density and/or geometric overlap (track-to-track, layer-to-layer) are insufficient, leaving planar unbonded interfaces; balling stems from Plateau–Rayleigh breakup of a thin molten powders and is promoted by high scan speed/low line energy, poor wettability, and steep surface-tension (Marangoni) gradients; keyholing occurs when peak irradiance drives recoil pressure above a threshold, creating a vapor cavity whose collapse leaves deep, near-spherical/chain pores and a high depth-to-width ("teardrop") fusion zone. In our DPM, the step and dwell point exposures with 450 nm diodes yield efficient absorption and wider, more equiaxed conduction mode pools at lower peak irradiance, while Dynamic Laser Area Heating (DLAH) raises the preheat level, reducing melt viscosity and thermal gradients, improving wetting and inter-track bonding; together these effects shrink the LOF window, suppress balling, and shift the process away from the keyhole regime for the same consolidation level. Keyhole was assessed by metallographic cross-sections (polished) taken normal and parallel to the scan direction across representative parameters, inspecting fusion-zone geometry and pore morphology; no deep, teardrop-shaped keyhole porosity or narrow, high-aspect melt pools were observed, whereas occasional pores at inter-track boundaries under under-energised settings were consistent with LOF.

During the examination of the Ti6Al4V samples produced with various process parameters, the balling and lack of fusion mechanisms are observed while the keyhole mechanism is not detected. Due to a lack of melting energy, some pores are noticeable in certain areas. Spatter – consisting of ejected molten metal droplets – is observed on some sample surfaces. This phenomenon occurs during laser melting and solidification of the metal powder bed, and may also involve partially sintered powders.

3.2. Effect of the position of the DPM laser without DLAH (Case-1 and Case-3)

In this section, the structures of Ti6Al4V samples produced with DPM lasers positioned at inclined and vertical position without using DLAH are examined for various scanning speeds. Fig. 9 presents the SEM and optical images of the samples for DPM lasers at vertical and inclined position. According to Fig. 9, which provides images at 200x magnification for SEM, when the scanning speed exceeds 1800 mm/min, spatter formation begins, and noticeable material defects appear. In the production with DPM lasers positioned both vertically and inclined, lack of fusion defect type is observed, particularly at scanning speeds above 2400 mm/min. When the scanning speed exceeds 4000 mm/min, significant pore formation is noted in the material. Comparing the SEM images of samples produced with vertical and inclined lasers clearly shows that the samples made with inclined lasers have more pronounced defect than those produced with vertical lasers. This difference is particularly noticeable at higher scanning speeds.

The defects observed in the structures of single layer samples directly affect material characteristics such as surface roughness and relative density. Fig. 10a presents the relative density values of samples produced with lasers positioned both inclined and vertically, based on various scanning speeds and NED values. According to the figure, the relative density values for the vertical case range from 96.80 % to 99.98

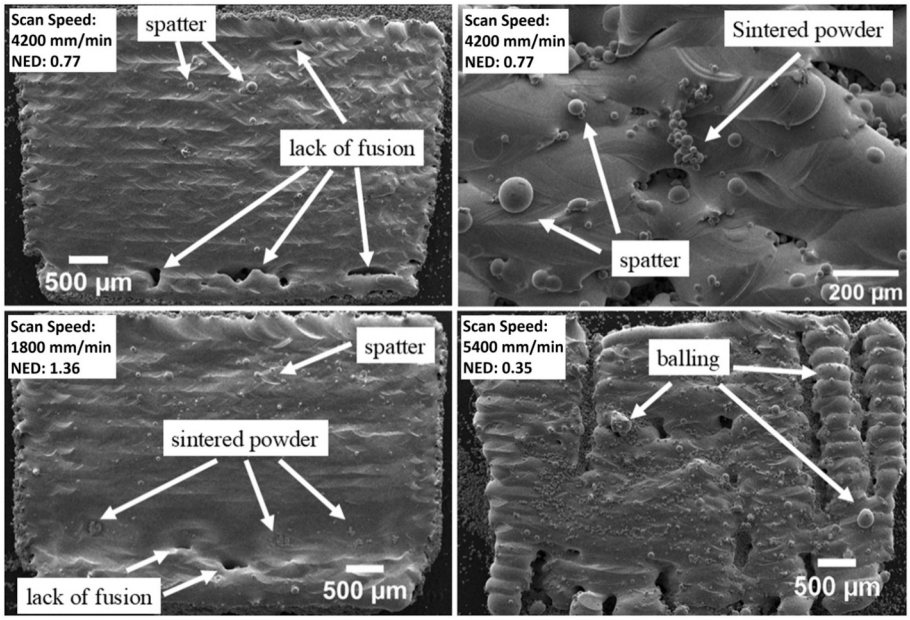

Fig. 8. The defects of Ti6Al4V samples produced with DPM and with/without DLAH lasers.

%, while for the inclined configurations, this range is between 93.79 % and 99.88 %.

At a scanning speed of 120 mm/min, the relative densities of the inclined and vertical laser configurations are 99.88 % and 99.94 %, respectively. For scanning speeds up to 2400 mm/min, both configurations maintain relative densities above 99 %. However, at 3600 mm/min, the densities decrease to 97.19 % (inclined) and 95.41 % (vertical), and at 4800 mm/min to 93.79 % and 96.80 %, respectively. As shown in Fig. 10a, increasing scanning speed reduces the NED, leading to a decline in density. Specifically, as the NED decreases from 20.42 to 0.51, the density drops from 99.94 % to 96.80 % in the vertical configuration and from 99.88 % to 93.79 % in the inclined configuration, corresponding to reductions of 3.14 % and 6.09 %, respectively.

Fig. 10b shows the surface roughness of the Ti6Al4V samples produced with DPM lasers at inclined and vertical positions for various scanning speed and NED values. According to the figure, the surface roughness values for the vertical case range from 6.2 to 48.34 µm, while for the inclined configurations, this range extends from 8.97 to 61.49 µm. As depicted in Fig. 10b, the surface roughness values increase with the laser scanning speed for both vertical and inclined configurations. For example, an inclined DPM laser exhibits a surface roughness of 8.97 µm at 1800 mm/min, which rises to 32.28 µm at 3000 mm/min and reaches 61.49 µm at 4800 mm/min. Similarly, for the vertically positioned samples, the surface roughness values are 20.90 µm, 28.21 µm, and 40.73 µm at scanning speeds of 1800 mm/min, 3000 mm/min, and 4800 mm/min, respectively. When comparing vertical and inclined cases at the same scanning speeds, it is generally observed that the vertical samples exhibit lower surface roughness values. The case with the lowest surface roughness is found as 6.2 µm in the sample produced using a vertical laser configuration and a scanning speed of 1200 mm/min (i.e., NED = 2.04). However, the case exhibiting the highest surface roughness value is found as 61.48 µm at the maximum scanning speed of 4800 mm/min (i.e., NED = 0.51) with the laser positioned at an inclined angle.

Fig. 9 also displays the 10x magnification of optical microscope images for melt pools of single layer Ti6Al4V samples produced using DPM lasers at inclined and vertical position. Fig. 11 also presents melt pool depth graphs calculated from Fig. 9 images. In LPBF systems, the melt pool should exhibit a homogeneous distribution, smooth boundaries, and low porosity. In LPBF systems, the melt pool should exhibit a homogeneous distribution, smooth boundaries, and low porosity. Additionally, the size and shape of the melt pool can be significantly affected by the processing parameters.

Examination of the melt pool images shown in Fig. 9 which 10x optical images indicates that the scanning speed significantly influences the melt pool characteristics for single-layer samples. According to Fig. 9, significant melt pool fluctuations and considerable amounts of sintered but unmelted powder are observed in inclined configurations when the scanning speed exceeds 1800 mm/min. These melt pool instabilities may cause uneven powder spreading or inadequate melting for subsequent layers. As a result, porosity can progressively increase in multi-layered samples over time [27,28]. As the melt pool depth increases, the melt pool width may narrow and potentially cause issues such as keyhole mechanisms at low speeds and high laser powers. Therefore, maintaining a uniform melt pool is crucial for successful part production in laser-based manufacturing. According to Fig. 11, the melt pool depth values range from 147.59 to 321.11 µm for the vertical case, while for the inclined configurations, this range varies from 129.98 to 245.52 µm. When the DPM laser is positioned at an angle, it is observed that the melt pool depth increased as the scanning speed increased from 120 mm/min to 1800 mm/min. The maximum melt pool depth of 245.52 µm is recorded at a scanning speed of 1800 mm/min, while the minimum depth of 118.76 µm is observed at 4800 mm/min. When the DPM laser is in the vertical position, it is observed that as the scanning speed increases from 120 mm/min to 2400 mm/min, the melt pool depth also increases, reaching a maximum depth of 321.11 µm at this speed. Beyond this speed, the melt pool depth begins to decrease.

3.3. DPM processing with DLAH

3.3.1. Effect of DLAH presence for DPM laser in inclined position (Case-1 and Case-2)

In this section, the structures of Ti6Al4V samples produced with DPM lasers positioned at inclined position with using DLAH are examined for various scanning speeds. Fig. 12 presents the SEM and optical microscopy images of the samples with and without DLAH for DPM lasers in inclined position. According to the figure, when the heat laser is inactive, no material defects are observed in the sample up to a laser scanning speed of 1800 mm/min. However, beyond 1800 mm/min, more pores and unmelted powders are observed in various regions of the

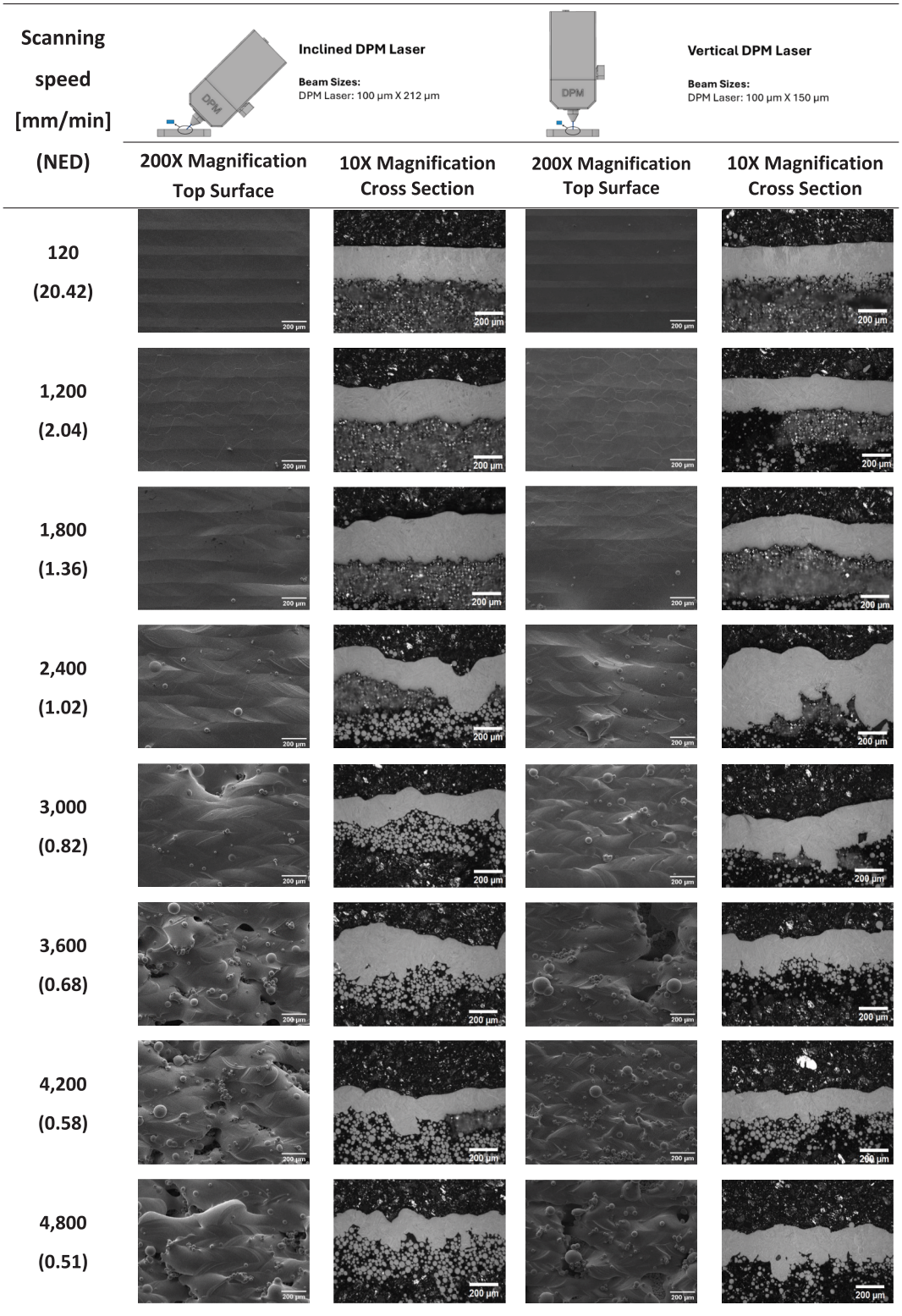

Fig. 9. SEM and optical microscopy images of Ti6Al4V samples produced without DLAH laser.

samples. When the DLAH is active, no defects are observed in the material at laser scanning speeds up to 3000 mm/min. Beyond laser scanning speed of 3000 mm/min, partial structural defect begins to appear. This indicates that the DLAH laser has a significant impact on the melting characteristics of the powder. This can also be clearly seen from the relative density and surface roughness values presented in Fig. 13.

Fig. 13 presents the relative density values obtained from the SEM images and surface roughness values. As seen in Fig. 13, up to a laser speed of 3000 mm/min, the samples with DLAH exhibit higher relative density values compared to those without DLAH. Specifically, at a laser speed of 120 mm/min, the relative density of the sample without DLAH is 99.88 %, whereas with the DLAH laser active, this value reaches 99.99 %. Similarly, without DLAH, the relative density values at laser scanning speeds of 1200, 1800, and 2400 mm/min are 99.46 %, 99.10

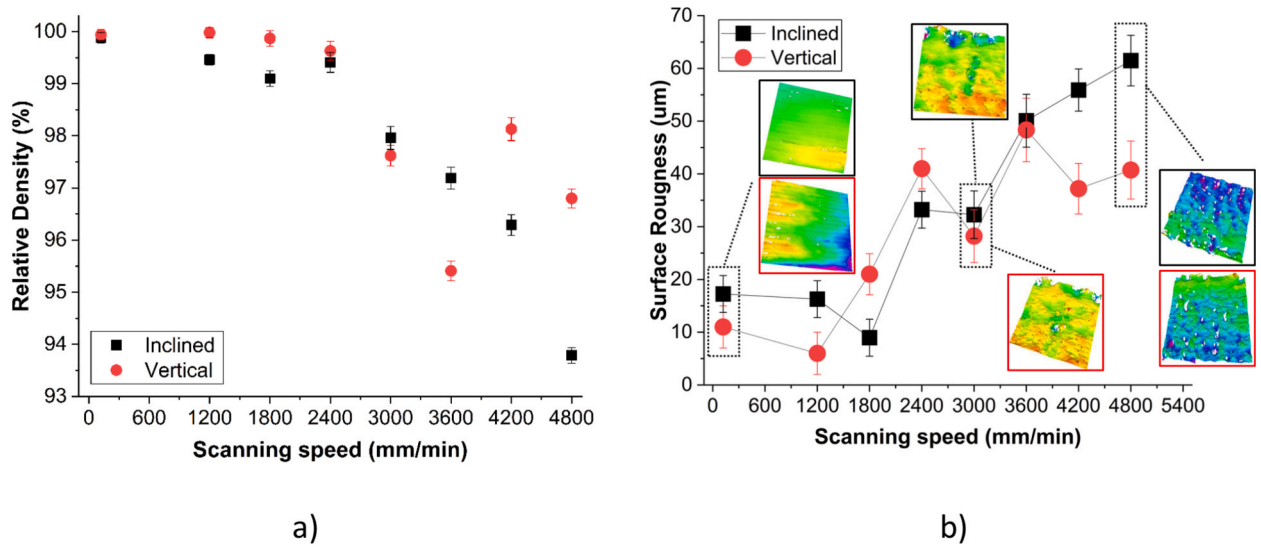

Fig. 10. a) Relative density and b) surface roughness comparison of DPM laser in inclined and vertical position for different scanning speeds.

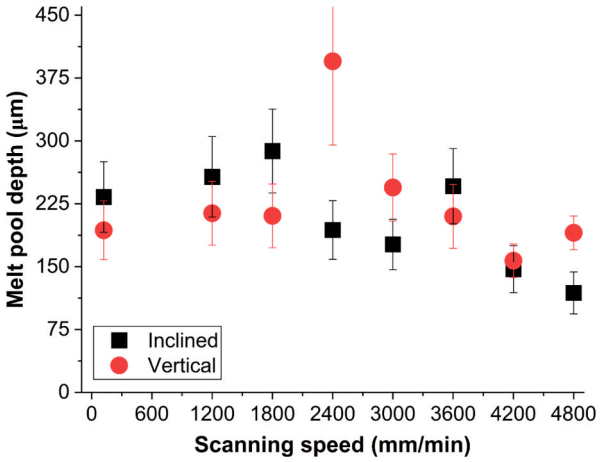

Fig. 11. Melt pool depth comparison of DPM laser in inclined and vertical position for different scanning speeds.

%, and 99.41 %, respectively, while with the DLAH laser active, these values increase to 99.99 %, 99.95 %, and 99.92 %. The highest relative density values, at 99.99 %, are achieved when the DLAH laser is active and the laser scanning speeds are 120 mm/min and 1200 mm/min. Additionally, when comparing based on NED values, it is clear that the samples with active heat consistently have the highest relative density values. Fig. 13 also presents the top surface roughness values of Ti6Al4V samples at different laser scanning speeds. Unlike the SEM images and relative density values, it is apparent that the surface roughness values with DLAH are significantly lower (i.e., better) compared to those without DLAH for all laser scanning speed and NED values. This improvement can be attributed to the reduction in thermal gradients induced by DLAH, which leads to a more thermally stable melt pool [29]. A reduced thermal gradient minimizes Marangoni convection-driven turbulence, promoting a smoother and more controlled fluid flow within the melt pool. Consequently, this stabilizes the melt pool boundaries and reduces the likelihood of process-induced instabilities such as spatter, balling, and ripple formation. Moreover, the smoother thermal profile enhances wettability by lowering the surface tension differential and decreasing melt viscosity, which collectively contribute to improved melt spreading and interlayer bonding [30].These conditions foster more uniform solidification fronts, reducing localized solidification defects and promoting a more homogeneous layer formation, thereby resulting in superior surface quality.

The surface roughness measurements demonstrate significant improvement when using DLAH across all tested scanning speeds (120–4800 mm/min). As shown in Table 4, DLAH activation reduced roughness values by 39.7–85.5 %, with the most dramatic improvements (67–85 % reduction) occurring at mid-range speeds (1200–3600 mm/min). The optimal combination occurred at 1200 mm/min, achieving both the lowest surface roughness (2.84 µm) and highest relative density (99.99 %, Fig. 13).

Fig. 12, optical images at 10x magnification and Fig. 14 display optical microscope images of melt pools and melt pool depth values for single layer Ti6Al4V samples produced using DPM lasers in inclined and vertical position. Fig. 12 shows that, particularly at high scanning speeds, the melt pool depth is greater and exhibits a significantly more irregular and wavy form when DLAH is not active. In contrast, when the DLAH laser is active, the melt pool depth decreases and becomes more uniformly distributed. Although the combined use of DLAH and DPM lasers increases total energy input, it results in a reduced average melt pool depth. This counterintuitive behaviour arises from the suppression of steep thermal gradients, which diminishes Marangoni convection and recoil-driven penetration [31]. As a result, the melt pool becomes more laterally spread and stable, with reduced turbulent flow and downward momentum. Additionally, DLAH laser partially sinters the powder bed, increasing thermal conductivity and altering optical properties such as absorptivity and scattering. These changes promote uniform lateral energy distribution rather than deep energy penetration, further contributing to a shallower but more uniform melt pool. This improved thermal and fluid dynamic environment reduces surface waviness, enhances melt track continuity, and improves layer stability [4,32]. This trend is also reflected in the graphs shown in Fig. 14. It presents the melt pool depth values for different laser scanning speeds and NED values, both with the DLAH laser active and passive. At a scanning speed of 120 mm/min, the melt pool depth of the sample without DLAH is higher than that of the sample with DLAH. However, when the laser speed increases to 1200 mm/min, the positive effects of DLAH begin to emerge, and at nearly all laser scanning speeds, the melt pool depth of the samples with DLAH is lower. Figs. 12 and 14 clearly demonstrate that DLAH significantly improves material quality, particularly in terms of relative density enhancement and surface roughness reduction.

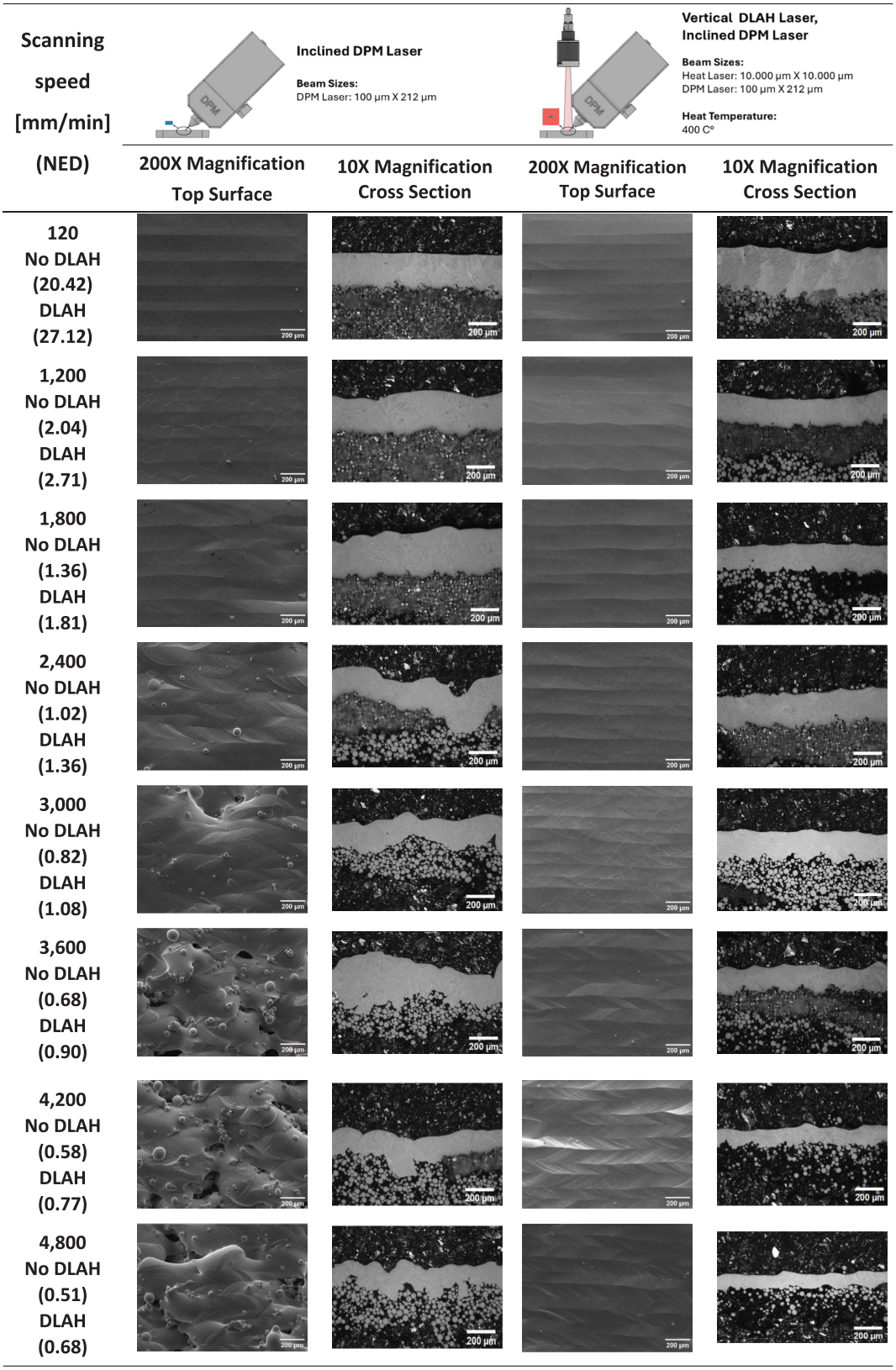

Fig. 12. SEM and optical microscopy images of Ti6Al4V samples produced with and without DLAH for DPM laser in inclined position.

3.3.2. Effect of DLAH inclined and DPM laser in vertical position (Case-3 and Case-4)

In this section, the structures of Ti6Al4V samples produced using DPM lasers positioned vertically and with DLAH are analysed at different scanning speeds. Fig. 15 displays the SEM images of samples produced with DPM lasers in vertical position, both with and without DLAH. Fig. 16 illustrates that when the DLAH laser is deactivated, the relative density values range from 95.41 % to 99.98 %. However, with

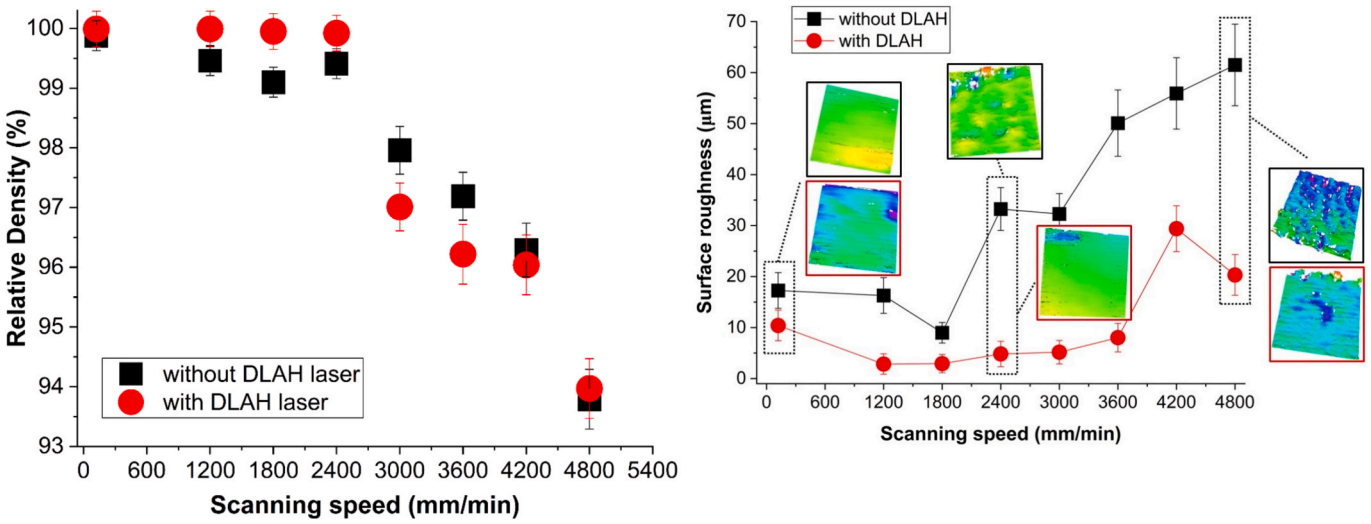

Fig. 13. Relative density and surface roughness comparison of DPM laser in inclined position with and without heat laser for different scanning speeds.

Table 4
Surface roughness measurements with and without DLAH activation at varying scanning speeds, showing percentage improvements.

Scanning Speed (mm/min)	Without DLAH (µm)	With DLAH (µm)	Reduction (%)
120	17.25	10.40	39.72
1200	16.28	2.84	82.56
1800	8.97	2.93	67.37
2400	33.24	4.82	85.50
3000	32.28	5.15	84.03
3600	50.09	8.01	84.00
4200	55.90	29.39	47.43
4800	61.49	20.30	66.98

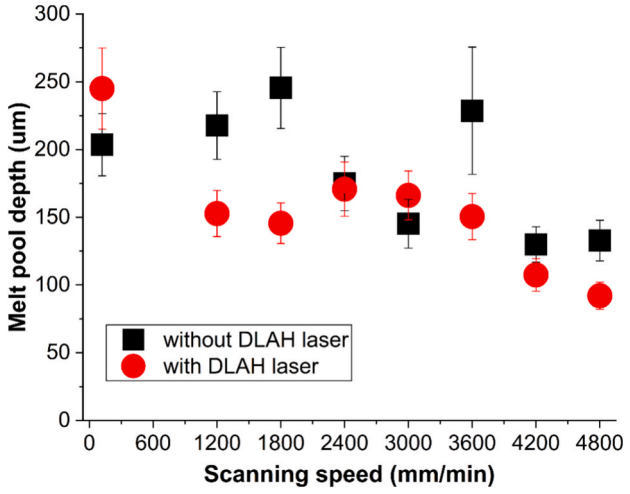

Fig. 14. Melt pool depth comparison of DPM laser in inclined position with and without heat laser for different scanning speed and normalised energy density.

the DLAH activated, the relative density values are between 97.05 % and 99.99 %. The scenario with the highest relative density of 99.99 % occurs when the DLAH laser is active, and the laser scanning speed is 1200 mm/min.

In Fig. 15, in the vertical scanning position without DLAH, no significant sample structural defect is observed up to a laser scanning speed of 1800 mm/min, but processing defects start to appear beyond this speed. When DLAH is activated, no significant defect is observed up to a laser scanning speed of 3600 mm/min. Especially at laser scanning speeds of 2400, 3000 and 3600 mm/min, the effectiveness of the DLAH laser on the microstructure is notably evident. Without the DLAH laser, spatter and balling mechanisms are more prevalent at these speeds. However, with DLAH active, such processing defects are considerably reduced. This effect is also evident in the relative density and surface roughness values shown in Fig. 16.

When the DLAH laser is inactive, the relative density values at laser scanning speeds of 3000 mm/min and 3600 mm/min are 97.62 % and 95.41 %, respectively. However, with the DLAH laser active, these values increase to 99.06 % and 98.84 %, respectively. Similarly, when examining the surface roughness values, the measurements for laser scanning speeds of 2400, 3000, and 3600 mm/min are 41.01, 28.21, and 48.34 µm, respectively, when DLAH is inactive. When active these values decrease to 8.32, 10.20, and 21.90 µm, respectively. This corresponds to an improvement in surface quality of approximately 79.70 %, 63.83 %, and 54.69 %. Additionally, for all laser scanning speeds, the scenarios with DLAH exhibit lower (better) surface roughness values compared to those without DLAH. The scenarios with the lowest surface roughness values occur at a laser scanning speed of 1200 mm/min, both with and without DLAH. In both cases, the surface roughness value is approximately 6 µm.

SEM and optical microscopy images of Ti6Al4V samples produced with/without DLAH for DPM laser in vertical position are shown in Fig. 15. Similar to the case where the DPM laser is inclined, when the DPM laser is positioned vertically, the melt pool characteristics of the produced Ti6Al4V samples show significant improvement for various laser scanning conditions. For instance, at a laser scanning speed of 1800 mm/min, the sample cross-section, which exhibits a wavy form when the DLAH laser is inactive, becomes more uniform with the activation of DLAH.

The melt pool depth graph is presented in Fig. 17. According to this graph, at a laser scanning speed of 120 mm/min, the melt pool depth is 270.92 µm when the DLAH laser is active, compared to 170.42 µm when it is inactive. This can also be seen in the optical microscope images in Fig. 20. As the laser scanning speed increases beyond 120 mm/min, the effects of DLAH on the microstructure of the material become more evident. For example, at laser scanning speeds of 1200, 1800, and 2400 mm/min, the melt pool depth is 186.33, 184.87, and 321.11 µm, respectively, when the DLAH laser is inactive. When the DLAH laser is active, these values are reduced to 134.93, 100.47, and 125.57 µm, respectively. Among all cases in Fig. 19, the lowest melt pool depth of 100.47 µm occurs at an NED value of 1.36 with the DLAH laser active, while the highest melt pool depth of 147.59 µm is observed at an NED

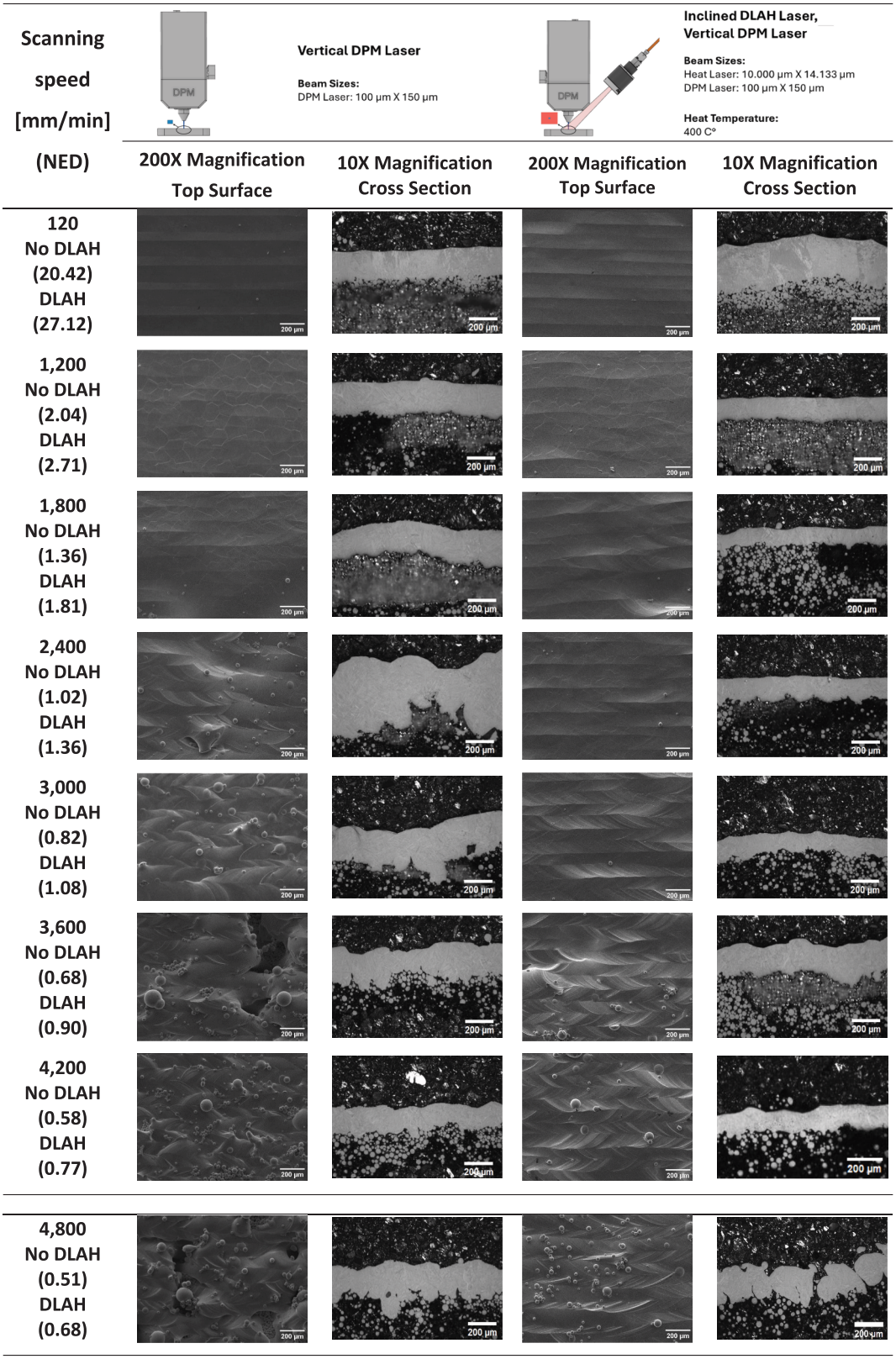

Fig. 15. SEM and optical microscopy images of Ti6Al4V samples produced without and with DLAH laser for DPM laser in vertical position.

value of 0.58 without DLAH.

In summary, for both vertical and inclined DPM laser configurations, the use of a DLAH laser results in significant improvements in the relative density, surface roughness, and melt pool characteristics of the produced samples. With DLAH, the relative density increases to as high as 99.99 %, and the surface roughness values decrease to as low as 2.84 µm. Furthermore, examination of the sample cross-sections reveals that DLAH transforms the melt pool region from a wavy to a more uniform form. This examination also provides important findings that each layer top surface will be more parallel with DLAH in multilayer production

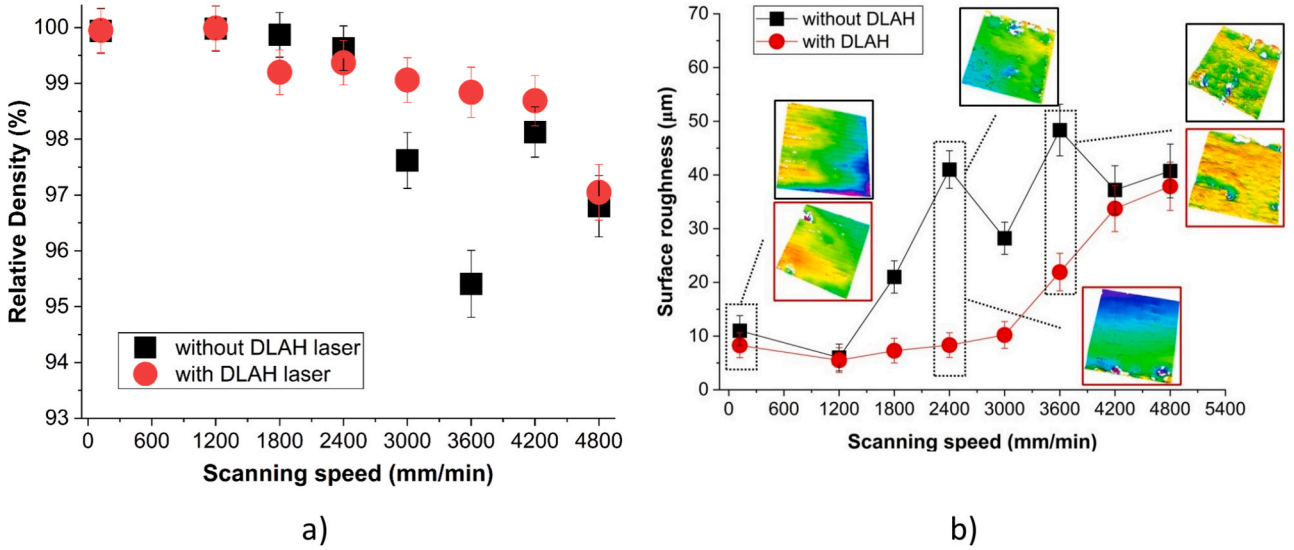

Fig. 16. A) relative density and b) surface roughness comparison of DPM laser in vertical position with and without DLAH for different scanning speeds.

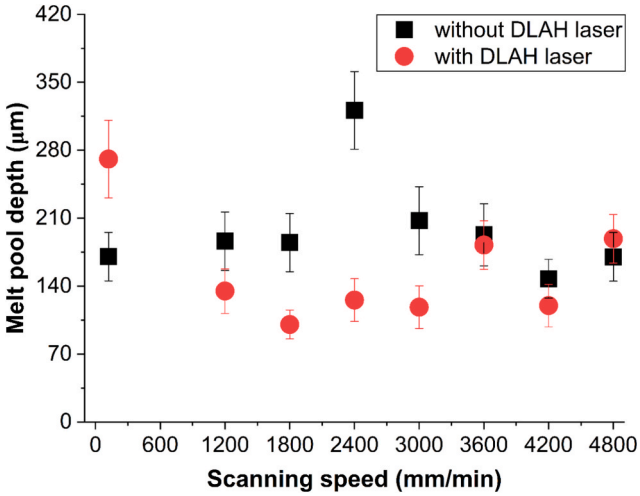

Fig. 17. Melt pool depth comparison of DPM laser in vertical position with and without DLAH for different scanning speed and normalised energy density.

and the porosity and defects that may occur between each layer will decrease.

3.4. Optimal positions for DPM/DLAH lasers (Case-2 and Case-4)

Previous sections demonstrate that DLAH significantly improves surface finish, increases relative density, and stabilizes melt pool characteristics. This section examines Ti6Al4V samples produced with the DLAH laser active, considering both vertical and inclined positions of the DPM laser. Since earlier chapters present SEM and optical images, this section focuses solely on the graphs for relative density and surface roughness. Fig. 18 presents a comparison of relative density and surface roughness for the DPM laser in inclined and vertical positions, with DLAH laser, across various scanning speeds and NED. From the figure, it is observed that for laser scanning speeds up to 3000 mm/min with the DPM laser in the vertical position, and up to 2400 mm/min with the DPM laser in the inclined position, the relative density values exceed 99 %. However, as the laser scanning speed increases further, a reduction in relative density values is observed. The highest relative density values for all cases occur when the NED values are 20.4 and 2.04, and the laser scanning speeds are 120 and 1200 mm/min, respectively, with the DPM laser in the inclined position. Similarly, the same relative density of 99.99 % is achieved when the DPM laser is in the vertical position, with an NED value of 2.04 and a laser scanning speed of 1200 mm/min. For

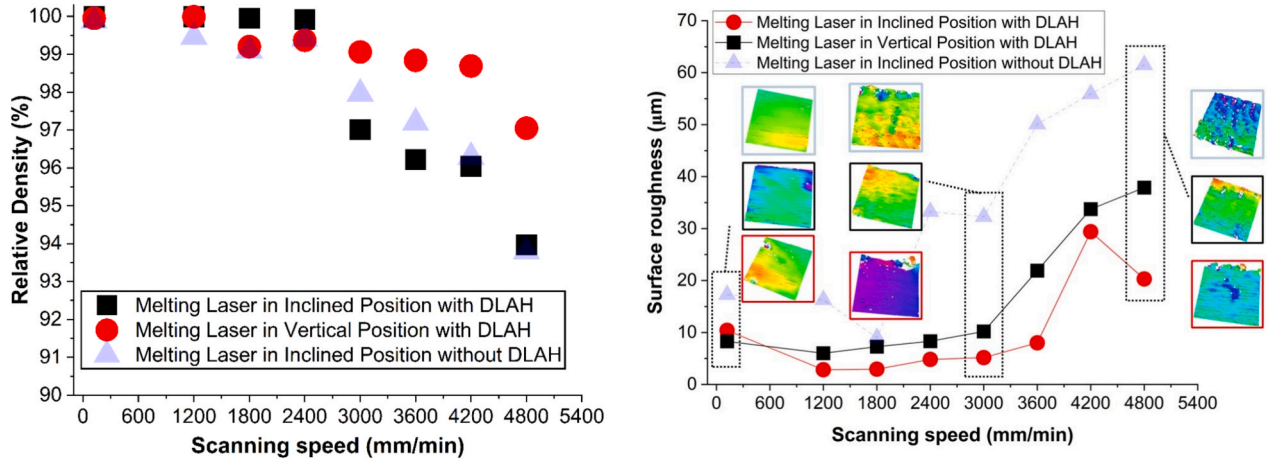

Fig. 18. Relative density and surface roughness comparison of DPM laser in inclined and vertical position with heat laser for different scanning speeds.

DLAH-activated scenarios, surface roughness values differ significantly between vertical and inclined DPM laser positions. While this positional effect is more pronounced for surface roughness, relative density also shows measurable differences at higher scanning speeds. For all NED values except 20.4 (at a laser scanning speed of 120 mm/min), lower surface roughness values are obtained when the DPM laser is positioned vertically. The lowest surface roughness value of 2.84 μm is observed when the DPM laser is in the vertical position with an NED value of 2.04. To clearly illustrate the impact of DLAH on the material's surface roughness, the worst-case scenario where the DPM laser is in the inclined position and DLAH is not used is included in Figs. 18 and 19. The figure demonstrates that the DLAH laser significantly impacts the microstructures of the Ti6Al4V samples and achieves a notable improvement in surface roughness values. Specifically, for a NED value of 1.02 (i.e., a laser scanning speed of 2400 mm/min), the surface roughness with DLAH is found to be 6.89 times lower compared to the condition without DLAH.

3.5. Microstructural customisation

The XRD analysis results of samples produced at speeds of 120, 1800, and 3000 mm/min are presented in Fig. 19. According to these results, at the speeds of 120 mm/min and 1800 mm/min, positive peaks corresponding to the β-phase were observed in the crystal orientation of 110 when heat is active. This indicates a much slower cooling rate and a trend towards an increase in the β-phase. However, in scenarios where the speed exceeded 3000 mm/min, the combined movement of the melting (DPM) and heating (DLAH) lasers resulted in insufficient time

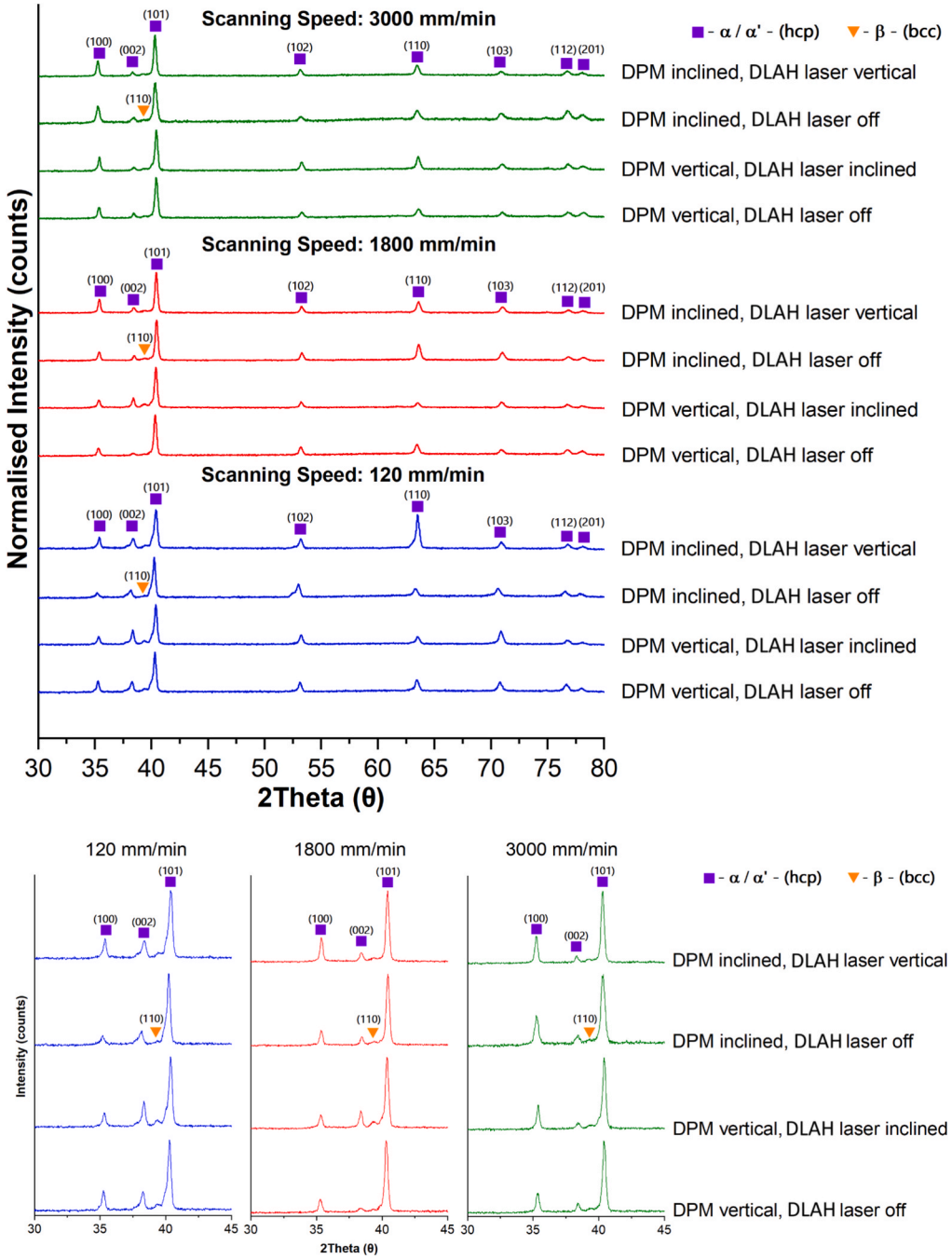

Fig. 19. XRD analysis of samples 120 mm/min, 1800 mm/min and 3000 mm/min speed conditions.

for the DLAH laser to effectively heat the surface due to the high speed, thereby not contributing adequately to reducing the cooling rate. This situation is also reflected in the XRD results, where no significant change in the β-phase corresponding to the crystal orientation of 110 is observed.

The evolution of martensitic microstructures in Ti6Al4V produced via DPM and DLAH laser was investigated under four distinct case configurations illustrated in Fig. 20. These configurations were

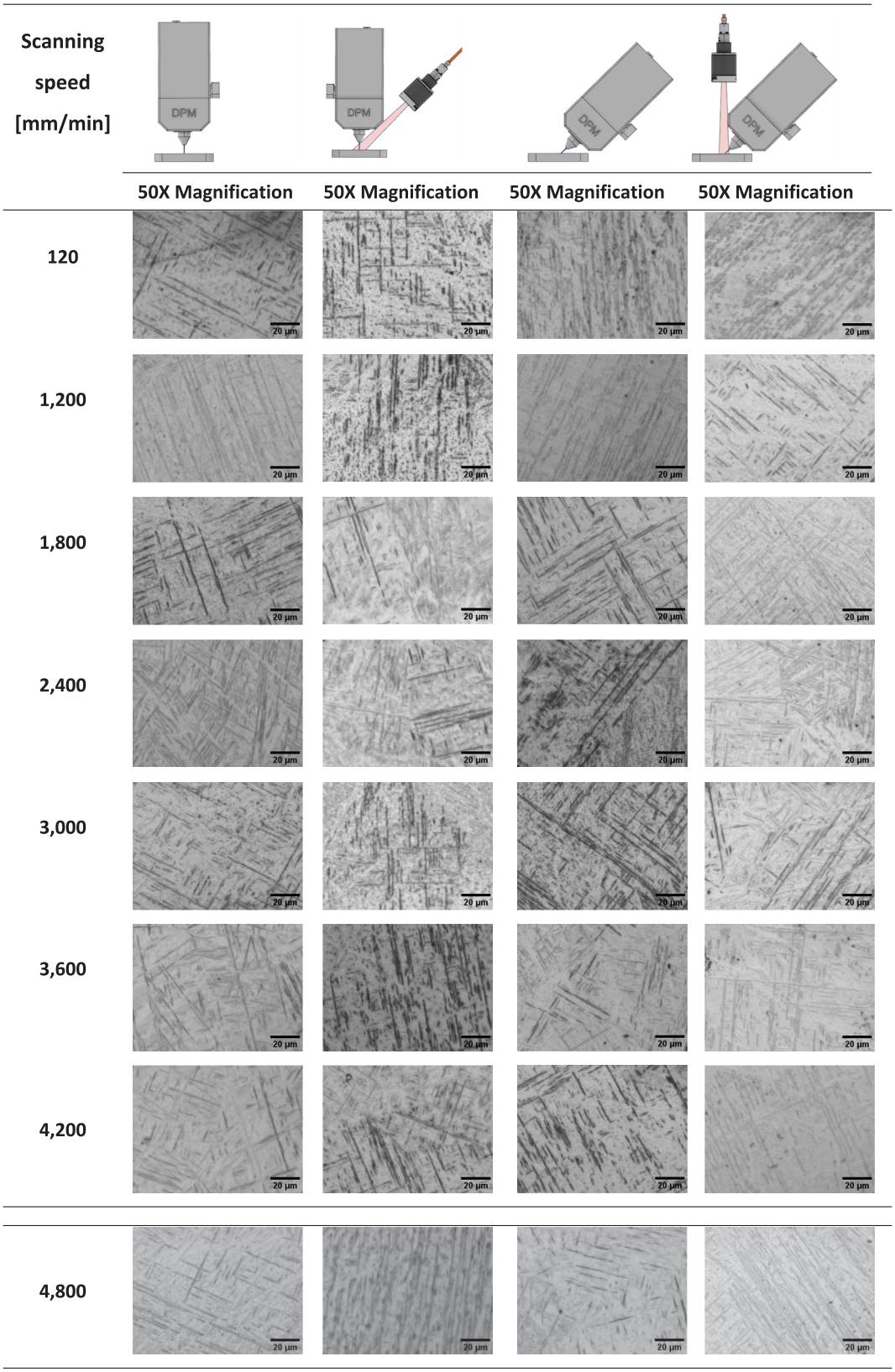

Fig. 20. Optical microscopy of etched images of Ti6Al4V samples in different conditions.

categorised into two principal groups based on the presence or absence of auxiliary DLAH laser heating. A systematic study was conducted across scan speeds ranging from 2 mm/s to 80 mm/s to evaluate the influence of process thermodynamics and scan strategy on the morphology of martensitic α′ laths. The primary objective was to quantify the geometric parameters of the martensitic structure namely lath length, width, and aspect ratio and to interpret the influence of thermal gradients induced by melting and heating directions on the resultant microstructure.

In the absence of external laser heating (Case 1 and Case 3), the high thermal gradients generated by the rapid localised melting produced a rapid solidification front, thereby favouring the formation of fine acicular α′ martensite similar to Refs [33–35]. In particular, the inclined melting laser condition consistently exhibited vertically aligned and slender α′ structures with limited retained β-phase presence. The average lath widths in the no-heating group remained below 2.6 μm across all speeds, while aspect ratios generally exceeded 2.8, indicative of needle-like, high aspect-ratio martensite. The vertical melting laser configuration, where the melting path was directed vertically, resulted in a relatively uniform basketweave martensitic microstructure, particularly pronounced at intermediate scan speeds. The unidirectional thermal flow in vertical melting laser led to well-defined columnar growth of martensitic packets, with minimal morphological disruption. In contrast, the inclusion of laser-based heating in Case 2 and Case 4 configurations substantially altered the solidification conditions. The application of heating either during or prior to melting served to reduce the cooling rate by raising the ambient thermal field around the melt pool. This modification of the thermal gradient facilitated the coarsening of martensitic structures and occasionally allowed partial diffusion-driven transformations. The inclined heating laser condition, characterised by inclined heating and vertical melting, generated notably wider martensitic laths, particularly at low scan speeds. This reflects the extended solidification times and lower undercooling achieved via the angular diode laser. Eshawish et al. [35] investigated the influence of cooling rates following solution treatment on the microstructure of LPBF-fabricated Ti-6Al-4 V, demonstrating that slower cooling rates (air cooling and furnace cooling) promote more extensive β → α phase transformation, resulting in coarser α-lath structures. In the vertical laser heating configuration, where heating was applied vertically and melting occurred along an angular trajectory, the resultant microstructures were highly heterogeneous. The combined influence of non-uniform thermal exposure and off-axis scanning produced a complex mix of acicular and semi-equiaxed α′ morphologies, especially at moderate scan speeds.

The microstructural observations are quantitatively supported by Table 5 data. Across all conditions, DLAH configurations consistently produced wider α′ laths (average ~ 3.0 μm) with reduced aspect ratios (2.4–2.5), contrasting with the finer, elongated laths (width < 2.6 μm, aspect ratio > 2.8) formed under rapid solidification without DLAH. Notably, lath length remained stable (7.1–7.5 μm), indicating width/aspect ratio are more thermally sensitive than length. In summary, this study confirms that the inclusion of laser-based heating significantly alters the morphological characteristics of α′ martensite in DPM processed Ti6Al4V. Derimow et al. [34] investigated the effects of varying temperatures and cooling rates on the microstructure of LPBF-fabricated Ti6Al-4 V. Their results demonstrate that the cooling rate significantly influences the α lath morphology, affecting mechanical properties. While without DLAH conditions promote the formation of fine, high aspect ratio laths associated with rapid solidification and steep thermal gradients, DLAH introduces a more complex thermal environment that facilitates coarsening and structural heterogeneity. These findings are of particular importance for tailoring mechanical properties via microstructural control, as finer martensite is typically associated with increased strength, whereas coarser morphologies may offer improved ductility. Bartolomeu et al. [36] confirmed this outcome in their detailed review of LPBF-fabricated Ti6Al4V microstructures, revealing that the rapid cooling rates in LPBF result in the formation of acicular α′-martensite with a needle-like morphology. They also noted that post-processing heat treatments can adjust the α-lath thickness, ultimately influencing the material's strength and ductility. Moreover, Zhang et al. [37] emphasized in their study that an appropriate heat treatment can establish an optimal strength-ductility balance in LPBF-fabricated Ti–6Al–4 V specimens.

Table 5
Quantitative analysis of heating conditions.

Metric	Without DLAH Laser (Case 1 + 3)	With DLAH Laser (Case 2 + 4)
Mean lath length (μm)	7.21 ± 0.29	7.30 ± 0.24
Mean lath width (μm)	2.51 ± 0.18	3.02 ± 0.29
Mean aspect ratio	2.87 ± 0.10	2.47 ± 0.16
Lath count per image	~85–120	~75–110

3.6. Heating and oxidation of powder

In LPBF processes, oxidation of reactive alloying elements such as titanium and aluminium are a critical concern, especially under imperfect shielding conditions where residual oxygen levels remain in the inert argon environment. Even at oxygen concentrations below 0.1 vol% as maintained in this study, there is a thermodynamic driving force for oxide formation at elevated temperatures due to the high affinity of Ti and Al for oxygen [38]. The incorporation of a 915 nm DLAH laser introduced prolonged thermal exposure of the powder surface, raising the substrate and adjacent powder temperatures to approximately 400 °C. This increased exposure time and temperature could, in principle, enhance the diffusion and reaction rates between oxygen and exposed metal particles. However, several observations suggest that oxidation was mitigated or at least did not become detrimental under the tested conditions. Firstly, no evident oxide layers or increased surface defects were observed in SEM micrographs of samples produced with active heating, and relative density consistently exceeded 99 % in most conditions with heating, suggesting minimal inclusion-related porosity. Secondly, the DLAH beam was operated defocused with a quasi–top-hat power-density profile, delivering uniform, low-flux heating over a broad area. Beam-shaping analyses for LPBF show that flattening the intensity distribution broadens the surface-temperature plateau and reduces central overheating relative to Gaussian input, thereby reducing temperatures associated with evaporation/chemical decomposition; moreover, non-Gaussian profiles demonstrably lower evaporation losses by > 2.5 × compared with Gaussian beams [39]. In Ti-6Al-4 V, oxidation (α-case formation) intensifies with increasing temperature and time and tends to occur above ≈480 °C in oxygen-containing atmospheres, so moderating peak surface temperatures is consistent with reducing the thermodynamic/kinetic driving force for transient oxidation surges under otherwise similar conditions. While we did not quantify oxygen uptake in this study, the temperature-dependence of oxidation provides the mechanistic basis for this interpretation [40]. It is also worth noting that at elevated preheating temperatures (e.g., >400 °C), previous studies have observed a passive oxidation behaviour in Ti6Al4V due to the formation of a thin TiO_2 layer which can act as a barrier to further oxygen ingress [41,42]. The use of gas-atomised powder with low surface area and the short dwell time of the heating laser likely further limited oxidation kinetics. Overall, while laser heating increases thermal exposure of powder particles, its application in a tightly controlled low-oxygen argon atmosphere combined with uniform heating strategies appears to limit detrimental oxidation and does not compromise part integrity under the conditions evaluated.

Fig. 21 highlights a distinct difference between traditional LPBF studies and DPM laser studies based on their NED. Traditional LPBF studies, represented by blue ellipse, span a small range of NED values (4–32) and exhibit diverse process conditions, focusing on achieving

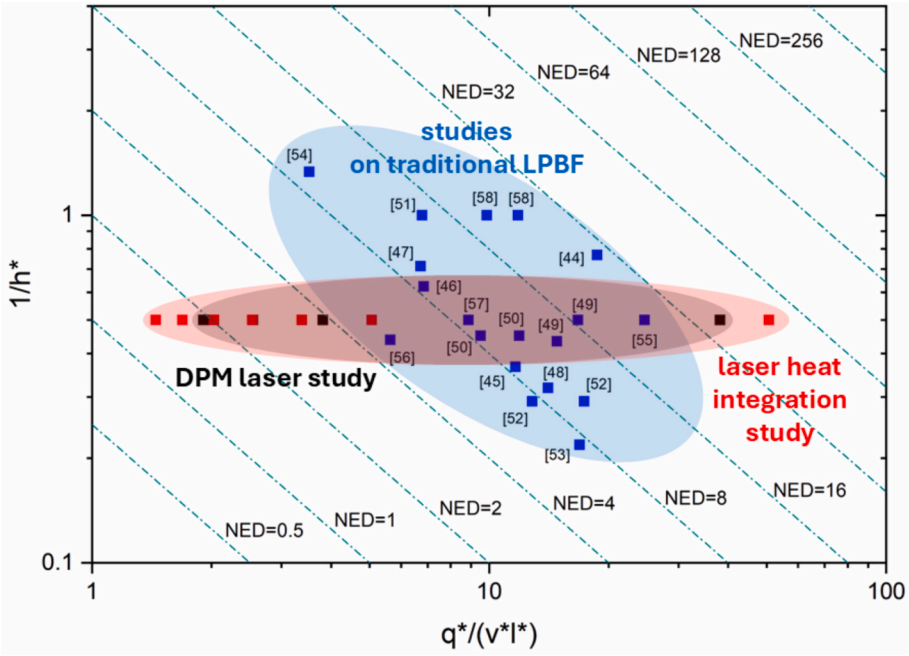

Fig. 21. Normalised energy density calculations, (blue region) traditional LPBF studies [43–57], (black region) DPM laser study and (red region) DPM & DLAH laser integration study. (For interpretation of the references to colour in this figure legend, the reader is referred to the web version of this article.)

optimized balance across mechanical properties, density, and thermal behaviour. In contrast, DPM laser studies, represented by a black ellipse and heating integration represented by a red ellipse, are concentrated in the wider NED region (<1, >32), This contrast demonstrates that while LPBF studies focus on specialized, energy-efficient processing methods with narrower operational windows, while DPM studies can explore a wider parameter space for general application.

4. Conclusions

This study investigated the integration of a new Dynamic Laser Area Heating (DLAH) within a powder bed fusion approach, Diode Point Melting (DPM. By employing a 44 W, 450 nm DPM laser in conjunction with a 140 W, 915 nm defocused heating laser (DLAH), the melt pool thermal gradient was reduced, enabling significant reductions in thermal gradients and process-induced defects. The process conditions achieved notable changes in part density, melt pool stability and microstructure coarsening. A maximum relative density of 99.99 % and a minimum surface roughness of 2.84 μm were obtained at a scanning speed of 1200 mm/min (normalised energy density, NED = 2.04) with the DPM laser in vertical orientation and DLAH activated. In contrast, in non-heated configurations, relative density decreased to ~93.8 %, and surface roughness exceeded 60 μm at higher scan speeds due to lack-of-fusion and increased spatter formation.

In addition to the improvements in densification and surface integrity, this study highlights the critical role of DLAH in enhancing melt pool stability and altering thermal-solidification dynamics. The application of spatially localised heating was found to substantially broaden the stable processing window, allowing higher scan speeds and lower energy densities without compromising melt pool continuity or inducing defect mechanisms such as balling or lack of fusion. This thermal stabilisation effect is particularly valuable for process scalability and reliability. However, the cooling rates derived from stationary measurements (19.6 °C/s) must be contextualised within the dynamic nature of scanning.

Microstructural analyses using X-ray diffraction and etched optical microscopy images confirmed that the inclusion of auxiliary DLAH in DPM-processed Ti6Al4V significantly alters the α′ martensite morphology by modifying thermal gradients and solidification conditions. In the absence of DLAH, the rapid solidification promoted by steep thermal gradients resulted in fine acicular laths with average widths consistently below 2.6 μm and aspect ratios exceeding 2.8, indicative of slender, needle-like structures. In contrast, DLAH configurations produced wider laths, averaging approximately 3.0 μm in several cases, with reduced aspect ratios in the range of 2.4–2.5, reflecting the effect of lowered cooling rates and extended solidification times. Despite these variations, the mean lath length remained relatively stable across all cases, ranging from 7.1 μm to 7.5 μm, indicating that length is less sensitive to thermal exposure.

Additionally, the impact of optical heating on oxidation was critically assessed. Although the 915 nm DLAH laser introduced prolonged thermal exposure, no deleterious oxidation or surface degradation was observed under the controlled argon atmosphere (O_2 < 0.1 %). SEM inspection revealed no oxide scale formation, and relative densities consistently exceeded 99 % across heated conditions. The use of a defocused top-hat beam profile contributed to thermal uniformity and limited localised oxidation kinetics, supporting safe application of preheating strategies for reactive materials.

In conclusion, this study demonstrates that integrating angularly coordinated DPM and DLAH laser in LPBF enables enhanced process control without compromising oxidation resistance. The findings validate that careful tuning of laser parameters supported by factorial statistical analysis can yield superior density, surface integrity, and phase stability in Ti6Al4V parts. This hybrid laser approach offers a viable, energy-efficient route for defect mitigation and microstructural tailoring in next-generation additive manufacturing of reactive alloys.

CRediT authorship contribution statement

Alkim Aydin: Writing – review & editing, Writing – original draft, Visualization, Validation, Methodology, Investigation, Formal analysis, Conceptualization. **Erhan Cetin:** Writing – review & editing, Writing – original draft, Visualization, Validation, Formal analysis. **Kamran Mumtaz:** Writing – review & editing, Supervision, Project administration, Funding acquisition, Conceptualization.

Declaration of competing interest

The authors declare that they have no known competing financial interests or personal relationships that could have appeared to influence the work reported in this paper.

Acknowledgements

This study was completed with support from the Turkish Government Ministry of Education, Cukurova University Unit of Scientific Research and Projects with project number FBA-2023-15352, TUBITAK-2219 postdoctoral fellowship support program with project number 1059B192300923 and UK Research and Innovation, Engineering and Physical Sciences Research Council Grant EP/W024764/1.

Data availability

The data that support the findings of this study are available from the corresponding author upon reasonable request.

References

[1] Z.-C. Fang, Z.-L. Wu, C.-G. Huang, C.-W. Wu, Review on residual stress in selective laser melting additive manufacturing of alloy parts, Opt. Laser Technol. 129 (2020) 106283, https://doi.org/10.1016/j.optlastec.2020.106283.
[2] C. Galy, E. Le Guen, E. Lacoste, C. Arvieu, Main defects observed in aluminum alloy parts produced by SLM: from causes to consequences, Addit. Manuf. 22 (2018) 165–175, https://doi.org/10.1016/j.addma.2018.05.005.
[3] Y.-H. Siao, C.-D. Wen, Examination of molten pool with Marangoni flow and evaporation effect by simulation and experiment in selective laser melting, Int. Commun. Heat Mass Transfer 125 (2021) 105325, https://doi.org/10.1016/j.icheatmasstransfer.2021.105325.
[4] J. Wang, R. Zhu, Y. Liu, L. Zhang, Understanding melt pool characteristics in laser powder bed fusion: an overview of single- and multi-track melt pools for process optimization, Adv. Powder Mater. 2 (2023) 100137, https://doi.org/10.1016/j.apmate.2023.100137.
[5] L. Caprio, A.G. Demir, G. Chiari, B. Previtali, Defect-free laser powder bed fusion of Ti–48Al–2Cr–2Nb with a high temperature inductive preheating system, J. Phys.: Photonics 2 (2020) 024001, https://doi.org/10.1088/2515-7647/ab7080.
[6] H. Ali, L. Ma, H. Ghadbeigi, K. Mumtaz, In-situ residual stress reduction, martensitic decomposition and mechanical properties enhancement through high temperature powder bed pre-heating of Selective Laser Melted Ti6Al4V, Mater. Sci. Eng. A 695 (2017) 211–220, https://doi.org/10.1016/j.msea.2017.04.033.
[7] D. Buchbinder, W. Meiners, N. Pirch, K. Wissenbach, J. Schrage, Investigation on reducing distortion by preheating during manufacture of aluminum components using selective laser melting, J. Laser Appl. 26 (2014), https://doi.org/10.2351/1.4828755.
[8] J. Gussone, Y.-C. Hagedorn, H. Gherekhloo, G. Kasperovich, T. Merzouk, J. Hausmann, Microstructure of γ-titanium aluminide processed by selective laser melting at elevated temperatures, Intermetallics (barking) 66 (2015) 133–140, https://doi.org/10.1016/j.intermet.2015.07.005.
[9] L. Papadakis, D. Chantzis, K. Salonitis, On the energy efficiency of pre-heating methods in SLM/SLS processes, Int. J. Adv. Manuf. Technol. 95 (2018) 1325–1338, https://doi.org/10.1007/s00170-017-1287-9.
[10] R. Casati, M.H. Nasab, M. Coduri, V. Tirelli, M. Vedani, Effects of platform pre-heating and thermal-treatment strategies on properties of alsi10mg alloy processed by selective laser melting, Metals (basel) 8 (2018) 954, https://doi.org/10.3390/met8110954.
[11] J. Böhm, C. Breuning, M. Markl, C. Körner, A new approach of preheating and powder sintering in electron beam powder bed fusion, Int. J. Adv. Manuf. Technol. 133 (2024) 3769–3784, https://doi.org/10.1007/s00170-024-13966-1.
[12] A. Lanzutti, E. Marin, The challenges and advances in recycling/re-using powder for metal 3D printing: a comprehensive review, Metals (basel) 14 (2024) 886, https://doi.org/10.3390/met14080886.
[13] A. Aydin, E. Cetin, S.C. Erman, K. Mumtaz, Laser powder bed fusion of Ti6Al4V using low-cost high efficiency 450 nm diode point melting, J. Mater. Res. Technol. 34 (2025) 2814–2827, https://doi.org/10.1016/j.jmrt.2024.12.252.
[14] H. Caglar, A. Aydin, I.T. Gulenc, K. Groom, K. Mumtaz, Dual-laser powder bed fusion using 450 nm diode area melting and 1064 nm galvo-scanning fiber laser sources, Mater. Des. 248 (2024) 113511, https://doi.org/10.1016/j.matdes.2024.113511.
[15] H. Caglar, A. Liang, K. Groom, K. Mumtaz, Multi-laser powder bed fusion of Ti6Al4V: diode area melting utilizing low-power 450 nm diode lasers, J. Mater. Process. Technol. (2024) 118303, https://doi.org/10.1016/j.jmatprotec.2024.118303.
[16] S.C. Erman, A. Aydin, K. Groom, K. Mumtaz, Diode area melting of SS316L using low power 450 nm lasers, Int. J. Adv. Manuf. Technol. 136 (2025) 4471–4490, https://doi.org/10.1007/s00170-025-15090-0.
[17] M. Alsaddah, A. Khan, K. Groom, K. Mumtaz, Use of 450-808 nm diode lasers for efficient energy absorption during powder bed fusion of Ti6Al4V, Int. J. Adv. Manuf. Technol. 113 (2021) 2461–2480, https://doi.org/10.1007/s00170-021-06774-4.
[18] Materials A. Titanium alloys - Ti6Al4V grade 5, 2002. https://Www.Azom.Com/Article. Aspx?ArticleID=1547.
[19] S.I.G. Fangaia, A. Messias, F.A.D.R.A. Guerra, A.C.F. Ribeiro, A.J.M. Valente, P.M. G. Nicolau, Evaluation of the Tribocorrosion Behavior of Ti-6Al-4V Biomedical Alloy in simulated Oral Environments, Processes 12 (2024) 1283, https://doi.org/10.3390/pr12071283.
[20] E. Cetin, A. Aydin, S.C. Erman, K. Mumtaz, in: Multi-Laser Powder Bed Fusion of Cu10Sn Using Low-Power 450nm Diode Lasers, University of Texas at Austin, Texas, 2024, pp. 1302–1317.
[21] J. Kónya, H. Hargitai, H. Jaber, P. Pinke, T.A. Kovács, Effect of surface modifications on surface roughness of Ti6Al4V alloy manufactured by 3D printing casting, and wrought, Materials 16 (2023) 3989, https://doi.org/10.3390/ma16113989.
[22] Z. Chen, J. Ye, N. Jin, K. Huang, Mechanical properties and microstructure evolution of Ti-6Al-4V prepared by selective laser melting in high layer thickness, Mater. Express 13 (2023) 1058–1067, https://doi.org/10.1166/mex.2023.2431.
[23] J. Karimi, C. Zhao, K.G. Prashanth, Massive transformation in dual-laser powder bed fusion of Ti6Al4V alloys, J. Manuf. Process. 119 (2024) 282–292, https://doi.org/10.1016/j.jmapro.2024.03.083.
[24] M. Thomas, G.J. Baxter, I. Todd, Normalised model-based processing diagrams for additive layer manufacture of engineering alloys, Acta Mater. 108 (2016) 26–35, https://doi.org/10.1016/j.actamat.2016.02.025.
[25] S. Chowdhury, N. Yadaiah, C. Prakash, S. Ramakrishna, S. Dixit, L.R. Gupta, D. Buddhi, Laser powder bed fusion: a state-of-the-art review of the technology, materials, properties & defects, and numerical modelling, J. Mater. Res. Technol. 20 (2022) 2109–2172, https://doi.org/10.1016/j.jmrt.2022.07.121.
[26] J.V. Gordon, S.P. Narra, R.W. Cunningham, H. Liu, H. Chen, R.M. Suter, J.L. Beuth, A.D. Rollett, Defect structure process maps for laser powder bed fusion additive manufacturing, Addit. Manuf. 36 (2020) 101552, https://doi.org/10.1016/j.addma.2020.101552.
[27] C. Ransenigo, M. Tocci, F. Palo, P. Ginestra, E. Ceretti, M. Gelfi, A. Pola, Evolution of melt pool and porosity during laser powder bed fusion of Ti6Al4V Alloy: numerical modelling and experimental validation, Lasers Manuf. Mater. Process. 9 (2022) 481–502, https://doi.org/10.1007/s40516-022-00185-3.
[28] E. Li, Z. Zhou, L. Wang, R. Zou, A. Yu, Modelling of keyhole dynamics and melt pool flow in laser powder bed fusion process, Powder Technol. 400 (2022) 117262, https://doi.org/10.1016/j.powtec.2022.117262.
[29] Y. Zhang, H. Ren, H. Yan, Y. Long, In situ study of surface morphology formation mechanism during laser powder bed fusion, Appl. Sci. 15 (2025) 2550, https://doi.org/10.3390/app15052550.
[30] M. Bayat, V.K. Nadimpalli, D.B. Pedersen, J.H. Hattel, A fundamental investigation of thermo-capillarity in laser powder bed fusion of metals and alloys, Int. J. Heat Mass Transf. 166 (2021) 120766, https://doi.org/10.1016/j.ijheatmasstransfer.2020.120766.
[31] A. Ur Rehman, M.A. Mahmood, F. Pitir, M.U. Salamci, A.C. Popescu, I. N. Mihailescu, Keyhole formation by laser drilling in laser powder bed fusion of Ti6Al4V biomedical alloy: mesoscopic computational fluid dynamics simulation versus mathematical modelling using empirical validation, Nanomaterials 11 (2021) 3284, https://doi.org/10.3390/nano11123284.
[32] N. Baldi, A. Giorgetti, M. Palladino, I. Giovannetti, G. Arcidiacono, P. Citti, Study on the effect of preheating temperatures on melt pool stability in inconel 718 components processed by laser powder bed fusion, Metals (basel) 13 (2023) 1792, https://doi.org/10.3390/met13101792.
[33] D.W. Brown, V. Anghel, L. Balogh, B. Clausen, N.S. Johnson, R.M. Martinez, D. C. Pagan, G. Rafailov, L. Ravkov, M. Strantza, E. Zepeda-Alarcon, Evolution of the microstructure of laser powder bed fusion Ti-6Al-4V during post-build heat treatment, Metall. Mater. Trans. A 52 (2021) 5165–5181, https://doi.org/10.1007/s11661-021-06455-7.
[34] N. Derimow, J.T. Benzing, H. Joress, A. McDannald, P. Lu, F.W. DelRio, N. Moser, M.J. Connolly, A.I. Saville, O.L. Kafka, C. Beamer, R. Fishel, S. Sarker, C. Hadley, N. Hrabe, Microstructure and mechanical properties of laser powder bed fusion Ti-6Al-4V after HIP treatments with varied temperatures and cooling rates, Mater. Des. 247 (2024) 113388, https://doi.org/10.1016/j.matdes.2024.113388.
[35] N. Eshawish, S. Malinov, W. Sha, Effect of solution treatment and cooling rate on the microstructure and hardness of Ti-6Al-4V alloy manufactured by selective laser melting before and after hot isostatic pressing treatment, J. Mater. Eng. Perform. 31 (2022) 3550–3558, https://doi.org/10.1007/s11665-021-06489-3.
[36] F. Bartolomeu, M. Gasik, F.S. Silva, G. Miranda, Mechanical properties of Ti6Al4V fabricated by laser powder bed fusion: a review focused on the processing and microstructural parameters influence on the final properties, Metals (basel) 12 (2022) 986, https://doi.org/10.3390/met12060986.
[37] M. Zhang, Y. Pan, K. Kang, T. Wang, D. Zhang, Ti–6Al–4V alloy prepared by laser powder bed fusion of a coarse powder, Heat Treat. Surf. Eng. 6 (2024), https://doi.org/10.1080/25787616.2024.2315716.
[38] M.J. Donachie, Titanium: A Technical Guide, 2nd edition, ASM International, 2000.
[39] S.N. Grigoriev, A.V. Gusarov, A.S. Metel, T.V. Tarasova, M.A. Volosova, A. A. Okunkova, A.S. Gusev, Beam shaping in laser powder bed fusion: péclet number and dynamic simulation, Metals (basel) 12 (2022) 722, https://doi.org/10.3390/met12050722.
[40] B. Öztürk, L. Mengis, D. Dickes, U. Glatzel, M.C. Galetz, Influence of water vapor and temperature on the oxide scale growth and alpha-case formation in Ti-6Al-4V

alloy, Oxid. Met. 97 (2022) 241–260, https://doi.org/10.1007/s11085-021-10088-x.
[41] C. Leyens, M. Peters, Titanium and Titanium Alloys: Fundamentals and applications, Wiley-VCH, 2003.
[42] F. Estupinán-López, C. Orquiz-Muela, C. Gaona-Tiburcio, J. Cabral-Miramontes, R. G. Bautista-Margulis, D. Nieves-Mendoza, E. Maldonado-Bandala, F. Almeraya-Calderón, A.J. Lopes, Oxidation kinetics of Ti-6Al-4V alloys by conventional and electron beam additive manufacturing, Materials 16 (2023) 1187, https://doi.org/10.3390/ma16031187.
[43] B. Vandenbroucke, J. Kruth, Selective laser melting of biocompatible metals for rapid manufacturing of medical parts, Rapid Prototyp. J. 13 (2007) 196–203, https://doi.org/10.1108/13552540710776142.
[44] J. Liu, Q. Sun, C. Zhou, X. Wang, H. Li, K. Guo, J. Sun, Achieving Ti6Al4V alloys with both high strength and ductility via selective laser melting, Mater. Sci. Eng. A 766 (2019) 138319, https://doi.org/10.1016/j.msea.2019.138319.
[45] Z. Li, I. Kucukkoc, D.Z. Zhang, F. Liu, Optimising the process parameters of selective laser melting for the fabrication of Ti6Al4V alloy, Rapid Prototyp. J. 24 (2018) 150–159, https://doi.org/10.1108/RPJ-03-2016-0045.
[46] S. Pal, N. Gubeljak, R. Hudak, G. Lojen, V. Rajtukova, J. Predan, V. Kokol, I. Drstvensek, Tensile properties of selective laser melting products affected by building orientation and energy density, Mater. Sci. Eng. A 743 (2019) 637–647, https://doi.org/10.1016/j.msea.2018.11.130.
[47] Y. Zhu, X. Chen, J. Zou, H. Yang, Sliding wear of selective laser melting processed Ti6Al4V under boundary lubrication conditions, Wear 368–369 (2016) 485–495, https://doi.org/10.1016/j.wear.2016.09.020.
[48] Ż.A. Mierzejewska, R. Hudák, J. Sidun, Mechanical properties and microstructure of DMLS Ti6Al4V alloy dedicated to biomedical applications, Materials 12 (2019) 176, https://doi.org/10.3390/ma12010176.
[49] Z. Wang, Z. Xiao, Y. Tse, C. Huang, W. Zhang, Optimization of processing parameters and establishment of a relationship between microstructure and mechanical properties of SLM titanium alloy, Opt. Laser Technol. 112 (2019) 159–167, https://doi.org/10.1016/j.optlastec.2018.11.014.
[50] X. Du, J. Chen, Y. She, Y. Liu, Y. Yang, J. Yang, S. Dong, Effect of process parameter optimization on morphology and mechanical properties of Ti6Al4V alloy produced by selective laser melting, Prog. Nat. Sci.: Mater. Int. 33 (2023) 911–917, https://doi.org/10.1016/j.pnsc.2024.01.006.
[51] W. Xu, M. Brandt, S. Sun, J. Elambasseril, Q. Liu, K. Latham, K. Xia, M. Qian, Additive manufacturing of strong and ductile Ti–6Al–4V by selective laser melting via in situ martensite decomposition, Acta Mater. 85 (2015) 74–84, https://doi.org/10.1016/j.actamat.2014.11.028.
[52] A. Fatemi, R. Molaei, S. Sharifimehr, N. Phan, N. Shamsaei, Multiaxial fatigue behavior of wrought and additive manufactured Ti-6Al-4V including surface finish effect, Int. J. Fatigue 100 (2017) 347–366, https://doi.org/10.1016/j.ijfatigue.2017.03.044.
[53] A. Khorasani, I. Gibson, M. Goldberg, G. Littlefair, On the role of different annealing heat treatments on mechanical properties and microstructure of selective laser melted and conventional wrought Ti-6Al-4V, Rapid Prototyp. J. 23 (2017) 295–304, https://doi.org/10.1108/RPJ-02-2016-0022.
[54] H. Amano, Y. Yamaguchi, T. Ishimoto, T. Nakano, Reduction of spatter generation using atmospheric gas in laser powder bed fusion of Ti–6Al–4V, Mater. Trans. 62 (2021) MT-M2021059, https://doi.org/10.2320/matertrans.MT-M2021059.
[55] B. Vrancken, L. Thijs, J.P. Kruth, J. Van Humbeeck, Heat treatment of Ti6Al4V produced by selective laser melting: microstructure and mechanical properties, J. Alloys Compd. 541 (2012) 177–185, https://doi.org/10.1016/j.jallcom.2012.07.022.
[56] S. Megahed, V. Aniko, J.H. Schleifenbaum, Electron beam-melting and laser powder bed fusion of Ti6Al4V: transferability of process parameters, Metals (basel) 12 (2022) 1332, https://doi.org/10.3390/met12081332.
[57] Y. Luo, M. Wang, J. Zhu, J. Tu, S. Jiao, Microstructure and corrosion resistance of Ti6Al4V manufactured by laser powder bed fusion, Metals (basel) 13 (2023) 496, https://doi.org/10.3390/met13030496.